Effect of High Pressure on the Crystal Structures of Polymorphs of l-Histidine

The Effect of High Pressure on the Crystal Structures of Polymorphs of *L*-Histidine

Giulia Novelli,[1] Helen E. Maynard-Casely,[2] Garry J. McIntyre,[2] Mark R. Warren[3] and Simon Parsons[*1]

1. EaStCHEM School of Chemistry and Centre for Science at Extreme Conditions, The University of Edinburgh, King's Buildings, West Mains Road, Edinburgh, Scotland, EH9 3FJ, UK.

2. Australian Nuclear Science and Technology Organisation, New Illawarra Road, Lucas Heights, NSW 2234, Australia.

3. Diamond Light Source, Harwell Campus, Oxfordshire, OX11 0DE, UK

The naturally occurring amino acid *L*-histidine exists as orthorhombic and monoclinic polymorphs. The hydrogen bonds in each are similar in terms of distance and energy, yet the response to pressure differs partly because of symmetry.

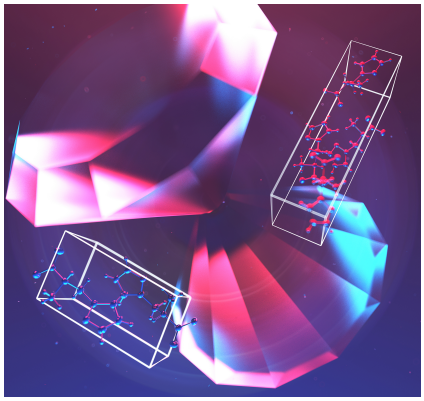

Abstract

The effect of pressure on the crystal structures of the two ambient-pressure polymorphs of the amino acid *L*-histidine has been investigated. Single-crystal diffraction measurements, up to 6.60 GPa for the orthorhombic form I ($P2_12_12_1$) and 6.85 GPa for the monoclinic form II ($P2_1$), show their crystal structures undergo isosymmetric single-crystal-to-single-crystal first-order phase transitions at 4.5 GPa and 3.1 GPa to forms I' and II', respectively. Although the similarity in crystal packing and intermolecular interaction energies between the polymorphs is remarkable at ambient conditions, the manner in which each polymorph responds to pressure is different. Form II is found to be more compressible than form I, with bulk moduli of 11.6(6) GPa and 14.0(5) GPa, respectively. The order of compressibility follows the densities of the polymorphs at ambient conditions (1.450 and 1.439 g cm^{-3}, for phases I and II, respectively). The difference is also related to the different space-group symmetry, the softer monoclinic form having more degrees of freedom available to accommodate the change in pressure. In the orthorhombic form, the imidazole-based hydrogen atom involved in the H-bond along the *c*-direction swaps the acceptor oxygen atom at the transition to phase I'; the same swap occurs just after the phase transition in the monoclinic form and is also preceded by a bifurcation. Concurrently, the H-bond and the long-range electrostatic interaction along the *b*-direction form a three-centred H-bond at the I to I' transition, while they swap their character during the II to II' transition. The structural data were interpreted using periodic-density-functional theory, symmetry-

adapted perturbation theory and semi-empirical Pixel calculations, which indicate that the transition is driven by minimisation of volume, the intermolecular interactions generally being destabilised by the phase transitions. Nevertheless, volume calculations are used to show that networks of intermolecular contacts in both phases are very much less compressible than the interstitial void spaces, having bulk moduli similar to moderately hard metals. The volume of the network actually expand over the course of both phase transitions, with the overall unit-cell-volume decrease occurring through larger compression of interstitial void space.

1. Introduction

High pressure is now a well-established way to study polymorphism and phase behaviour in molecular materials.[1–10] Nevertheless, there are relatively few diffraction studies where the response to pressure of the crystal structures of different polymorphs has been compared (Table S1 in the ESI). The first such investigation, a single-crystal X-ray diffraction study focused on forms I and II of the pharmaceutical compound paracetamol, was performed almost two decades ago.[11] The findings showed that the molecule is conformationally rigid, meaning that the crystal packing determines the differences between the polymorphs and their response to pressure. The bulk compressibilities were found to be qualitatively similar, yet substantial discrepancies in the anisotropy of structural distortion were observed.

Control of compressibility by intramolecular effects is rarer, but is observed in the highly polymorphic compound 5-methyl-2-[(2-nitrophenyl)amino]-3-thiophenecarbonitrile, known as ROY.[12] There are 11 known conformational polymorphs of this material at ambient conditions, nine of which were structurally characterised.[13] The piezochromic response of the 'yellow' (Y) and the 'orange-plate' (OP) forms were investigated using single-crystal X-ray and powder neutron diffraction.[14,15] No phase transition was observed up to 5.2 GPa in Y-ROY and 9.3 GPa in OP-ROY, though the former changed colour from yellow to red upon pressure increase. Their respective bulk moduli of 6.0(7) GPa and 4.3(3) GPa are low because of the flexible conformational geometry, whereas the wine-rack-style lattice deformation was identified as being the pivotal factor in the compression mechanism of OP-ROY.

Compressibility studies were also performed for the ambient-pressure polymorphs of the pharmaceutical compounds tolazamide,[16] pyrazinamide (PZA) and the energetic material 1,1-diamino-2,2-dinitroethene (FOX-7).[17,18] Forms I and II of tolazamide remained phase-stable up to 6.1 GPa and 6.8 GPa, respectively, although an incomplete form-II-to-form-I transition was detected at 0.1 GPa when a different pressure-transmitting medium was used. The bulk moduli were found to be similar, 6.4(3) GPa for form I and 5.8(2) GPa for form II. The effect of pressure on the α, δ and γ polymorphs of pyrazinamide (PZA) was explored up to 14 GPa using Raman spectroscopy and synchrotron X-ray powder diffraction. γ-PZA transformed at $\sim$4 GPa to β-PZA, which is also the least-stable ambient-pressure polymorph, while α-PZA and δ-PZA remained in the same phase throughout the experiments. The bulk moduli of the α, γ, β, δ-PZA polymorphs were found to span an unusually large range, 3.8(5), 6.3(4), 7.9(3) and 9.2(8) GPa, respectively, these values being determined by fitting to Murnaghan equations of state. Perdeuterated α-FOX-7 was investigated in a combined neutron powder diffraction and dispersion-corrected density-functional-theory study. A gradual phase transition to the ε-form was observed between 3.63 GPa and 4.24 GPa. The bulk moduli of the α-form obtained from the

experiment and the calculations were found to be in very good agreement, being respectively 11.8(5) and 12.5(2) GPa. A similar study performed using single-crystal X-ray diffraction found a bulk modulus of 10.1(7) GPa.[19]

The effect of pressure on hydrogen bonds has been studied extensively in the amino acids.[20] The simplest of them, glycine, has three ambient-pressure polymorphs, each of them showing a different compression behaviour. α-Glycine has been proven to remain in the same phase up to 6.2 GPa and 6.4 GPa by single-crystal X-ray and neutron powder diffraction respectively,[21,22] while X-ray powder diffraction measurements have shown that its stability extends to 50 GPa.[23] Conversely, β-glycine transforms to δ-glycine at only 0.8 GPa. γ-Glycine undergoes a gradual phase transition between 2.0 and 4.3 GPa to ε-glycine,[21,24] which reverses to its parent phase under decompression via the short-lived ζ-glycine.[25] The differences in the high-pressure behaviour have been ascribed to the orientational relationships between the molecules forming chains along the *c*-axis.[21] *L*-cysteine, which has a conformationally flexible side-chain, forms two ambient-pressure polymorphs, I and II. A combined neutron and X-ray single-crystal diffraction study showed that cysteine-I undergoes a phase transition to cysteine-III at 1.8 GPa, which transforms to cysteine-IV upon decompression to 1.7 GPa, before finally reverting to cysteine-I at ambient pressure.[26] Cysteine-III was found to be stable up to at least 4.2 GPa, which is in contrast with Raman results reported by Minkov *et al.*[27] where a phase transition was observed at 2.2 GPa. The discrepancy was interpreted in a subsequent study as being driven by different choices of compression paths.[28] Additionally, this investigation found reversible phase transitions in cysteine-II at 2.9 and 3.9 GPa. All the pressure-induced phase transitions in the *L*-cysteine polymorphs are related to changes in the H-bond network, but additionally in cysteine-I and –III there is a change in molecular conformation.

The high-pressure behaviour of the two ambient-pressure polymorphs of the amino acid *L*-histidine is the subject of the present study.[29,30] The crystal structures of the orthorhombic and monoclinic polymorphs have been determined by single-crystal X-ray diffraction up to 6.60 GPa and 6.85 GPa, respectively. Phase transitions are shown to occur in both polymorphs. The crystal packing and the intermolecular interaction energies are very similar in the two polymorphs at ambient conditions, but the way they respond to pressure is markedly different.

2. Experimental Section

2.1 Crystal Growth

Pure *L*-histidine-h_9 powder ($C_6H_9N_3O_2$, > 99%, Sigma-Aldrich), sodium hexametaphosphate powder (described as 'mainly $(NaPO_3)_6$, general purpose grade', Fisher Chemical) and ethanol (C_2H_5OH, analytical reagent grade, Sigma-Aldrich) were used without further purification.

Colourless, needle-shaped crystals of the orthorhombic polymorph were obtained from a solution of *L*-histidine (0.71 g) in deionised water (10 cm^3) by slow diffusion of ethanol. Colourless, plate-like crystals of the monoclinic polymorph were obtained from a solution of *L*-histidine (0.71 g) and sodium hexametaphosphate (0.8 g) in deionised water (10 cm^3) by slow diffusion of ethanol.[31]

2.2 Data Collection

Single-crystal diffraction data were collected for each polymorph of the amino acid *L*-histidine, at ambient pressure and 298 K, on an Agilent SuperNova diffractometer using Mo-Kα radiation (λ = 0.71073 Å).

High-pressure diffraction data were collected on Beamline I19-EH2 at the Diamond Light Source (Oxford, UK) with monochromated synchrotron radiation (λ = 0.4859 Å) using a Newport kappa-geometry 4-circle diffractometer fitted with a Dectris Pilatus 300 K pixel-array photon-counting detector.[32] In order to confirm reproducibility two crystals of the orthorhombic form were used for the measurements in the ranges ambient pressure to 5.61 GPa and 0.23 to 6.60 GPa, respectively. Similarly, two crystals of the monoclinic form were used in the pressure ranges ambient pressure to 5.77 GPa and 0.11 to 6.85 GPa, respectively. Additional data points at 0.97, 3.00, 3,21 and 5.20 GPa were also collected for a third crystal of the monoclinic polymorph on a Bruker D8 Venture diffractometer using Ag-Kα radiation (λ = 0.56083 Å). The crystal used for each data-set is specified in the ESI (Table S2).

In each case, the crystal was loaded into a Merrill-Bassett diamond-anvil cell (DAC) with half opening angle of 38°, 600 μm Boehler-Almax-cut diamonds and tungsten carbide backing plates.[33] A tungsten gasket of thickness 300 μm indented to 155 μm and hole diameter of 300 μm was used, along with a mixture of 4:1 methanol:ethanol as pressure-transmitting medium.[34] A small ruby chip was used as pressure calibrant and the ruby fluorescence method applied to measure the pressure.[35]

2.3 Structure Analysis

Ambient-pressure and synchrotron data were integrated in *CrysAlisPRO* or *SAINT*.[36,37] For synchrotron data, the unit-cell parameters used in structure refinement were obtained using *Xia2*.[38] Corrections for the DAC shading, absorption and other systematic errors were applied using the multi-scan procedures in *CrysAlisPRO* and *SADABS*.[39] The structures at ambient pressure were solved using dual-space methods (*SHELXT*) and subsequently refined by full-matrix least-squares on $|F|^2$ (*SHELXL*) within the *Olex2* graphical user interface.[40–42] Otherwise, refinements started from the atomic coordinates of the preceding pressure point. Intramolecular bond distances and angles in all refinements against high-pressure data were restrained, with uncertainties of 0.02 and 0.04 Å, respectively, to those of the structures at ambient conditions. The weighting scheme used was $w = 1/[\sigma^2(|F_o|^2)+(aP)^2]$, where $P = (|F_o|^2+2|F_c|^2)/3$ and a = 0.015 and 0.030 for ambient-conditions and high-pressure structures, respectively.[43,44] Where possible non-hydrogen atoms were refined with anisotropic displacement parameters and subject to rigid-bond restraints, otherwise structures were refined isotropically. Hydrogen atoms were placed in calculated positions and constrained to ride on their parent atoms. Crystal parameters, refinement statistics and data-collection details are given in Tables 1 and 2 for selected structures. Crystal and refinement data for all the structures collected in this work are available in Table S2 of the ESI, and are available from the Cambridge Crystallographic Data Centre, quoting deposition numbers 2020565-2020598.

2.4 Periodic-Density-Functional Theory (DFT) Calculations

Optimised structures for the two polymorphs, at 0 GPa and at high pressure, were computed using the plane-wave pseudopotential method in the *CASTEP* code.[45] The starting coordinates for optimisation were taken from the single-crystal X-ray refinements, the unit-cell parameters fixed to

the experimental values and the space-group symmetry retained. The Perdew-Burke-Ernzerhof (PBE) exchange-correlation functional was used, along with norm-conserving pseudopotentials and the Tkatchenko-Sheffler correction for dispersion.[46] The basis-set cut-off energy was 920 eV and Brillouin zone integrations were performed with a Monkhorst-Pack **k**-point grid spacing of 0.08 $Å^{-1}$.[47,48] The tolerances used for the cycles of geometry optimisation were 5×10^{-6} eV $atom^{-1}$ for energy convergence of a maximum force tolerance of 0.01 eV $Å^{-1}$ and maximum displacement tolerance of 5×10^{-4} Å. The self-consistent field convergence criterion was 5.0×10^{-7} eV $atom^{-1}$.

2.5 Intermolecular Interactions Energy Calculations

Pixel calculations[49–51] were carried out using the *MrPixel*[52] interface for all the structures using the *CLP-Pixel* suite.[51] The electron densities required for the calculations were obtained from *Gaussian-09*,[53] on a grid of dimensions $0.06 \times 0.06 \times 0.06$ $Å^3$ and with the 6-31G** basis set at the MP2 level of theory. The pixels were combined into $3 \times 3 \times 3$ blocks to save computational time. The structures investigated were those optimised by DFT in order to limit the effects of random errors in the experimental structure, and interactions within the cluster of radius 18 Å (25 Å for ambient pressure lattice energies) were considered in the calculations. Symmetry-adapted perturbation theory (SAPT) calculations were performed at the SAPT2+3 level of theory on dimers taken from the ambient and highest-pressure structures of the two polymorphs, using the *PSI4* code with the aug-cc-pvdz basis set.[54,55]

The total intermolecular interaction energies computed using the Pixel method were used to investigate the structural changes occurring upon compression of the two polymorphs of *L*-histidine. The total energy of each contact is the sum of contributions from Coulombic, polarisation, dispersion and repulsion interactions. The Pixel energies were validated against those of SAPT at ambient pressure and at the highest pressure for both polymorphs (Table 3 and 4). At ambient pressure, the absolute mean difference between Pixel and SAPT for the total energy is 3.5 kJ mol^{-1} in phase I and 3.0 kJ mol^{-1} in phase II, the corresponding figures at the highest pressure reached are 6.4 kJ mol^{-1} for both forms. While the absolute mean difference in the energy components results were higher in both polymorphs (Table S3 in the ESI), the two calculations always agree about the dominant energy term.

2.6 Volume Analysis

Molecular volumes were calculated using a Monte Carlo procedure. A molecule of histidine from the DFT-optimised crystal structure was placed inside a box (volume $= V_{box}$) large enough to contain it. The *x* dimension of the box was equal to $\Delta x_{o,max} + 2.5R_{vdw,max}$ where $\Delta x_{o,max}$ is the maximum difference between orthogonalised *x* coordinates and $R_{vdw,max}$ is the maximum van der Waals radius of the atoms in the structure. The *y* and *z* dimensions were calculated in the same way. A large number of random points (n_{total}) were generated inside the box. Any point within the van der Waals radius of an atom in the molecule was considered to lie inside the molecular van der Waals surface;[56] $n_{mol} =$ the number of these points. The volume of the molecule is then $V_{mol} = (n_{mol}/n_{total})V_{box}$. The procedure was repeated 16 times to test for consistency, and the values quoted below are the mean and standard deviation of the 16 results. It was found that values of $n_{total} = 10$ million yielded volumes with a reproducibility of ~0.1%. A similar procedure can be applied to the contents of one unit cell to identify the volumes of the network of intermolecular contacts (V_{net}) and interstitial void

spaces ($V_{void} = V_{cell} - V_{net}$), where V_{cell} = unit-cell volume. For the unit-cell calculations $n_{total} = 1$ million was found to be sufficient. The reason for the difference is that the standard deviation of the volume estimates varies as the inverse square-root of the number of points falling within the molecule or network.[57] The rather simple algorithm used to determine the box size in the molecular calculation resulted in the molecule occupying only ~15% of the box volume, whereas the figure for the unit-cell calculation was ~66% (the packing efficiency).

2.7 Other Programs Used

Mercury was used for data visualisation,[58] intramolecular and intermolecular geometries were analysed using *PLATON*.[59] Main directions of compressibility were calculated using *PASCal*.[60] Equation-of-state calculations were performed using the program *EOSFIT*.[61] During fitting, the zero-pressure volume (V_0) was fixed to experimental values [710.86(10) Å^3 in phase I and 358.10 (5) Å^3 in phase II], while the bulk modulus (K_0) and its first derivative (K') were refined. Weighted-χ^2 values of 1.26 and 1.29 were obtained for phase I and II, respectively. When the zero-pressure volumes were refined, their values of 714(3) Å^3 for phase I and 358.2(6) Å^3 for phase II are found in good agreement with, though somewhat less precise than, the experimental values.

3. Results and Discussion

3.1 Structural Relationship in the Polymorphs at Ambient Pressure

L-histidine-h_9 ($C_6H_9N_3O_2$, Figure 1a) exists as a zwitterion in the solid state with charged carboxylate and ammonium groups situated on the α-carbon (C2) and an imidazole ring linked to the β-carbon (C3). The amino acid forms two polymorphs under ambient conditions. Their crystal structures were first determined by Madden in 1972[29,30] and are available in the Cambridge Structural Database[62] as entries LHISTD01 and LHISTD10. The atom labelling used in this work is based on Madden's work and is given in Figure 1a. The orthorhombic polymorph which is obtained directly from aqueous solution, crystallises in the space group $P2_12_12_1$, with four molecules in the unit cell (Z' = 1) and unit-cell parameters: a = 5.1586(5) Å, b = 7.3367(6) Å, c = 18.7825(13) Å and V = 710.86(10) Å^3. The monoclinic polymorph, which forms from water in the presence of sodium hexametaphosphate, crystallises in space group $P2_1$, with two molecules in the unit cell (Z' = 1) and unit-cell parameters: a = 5.1698(4) Å, b = 7.3884(6) Å, c = 9.4715(7) Å, β = 98.177(5) ° and V = 358.10(5) Å^3. The cell dimensions suggest a close structural relationship between the phases. The orthorhombic form is often described as the thermodynamic phase at ambient temperature and pressure, while the monoclinic form is considered to be the kinetic phase.[63–65] We shall refer to the orthorhombic phase as phase I and the monoclinic phase as phase II. At ambient conditions, the lattice energy of phase I calculated using the Pixel method (−306.8 kJ mol^{-1}) is 3.6 kJ mol^{-1} more negative than that of phase II (−303.2 kJ mol^{-1}); when calculated using periodic DFT, the corresponding difference is only 0.1 kJ mol^{-1}.

The structure of the histidine molecule is shown in Figure 1b. Tables S4-6 in the ESI list and compare the experimental bond distances, valence and dihedral angles in the two polymorphs. Small differences are present in the dihedral angles (C2–C3–C4-N2, C2–C3–C4–C6, C3–C4–N2–C5 and C3–C4–C6–N3) that define the torsion of the imidazole ring about the alanine backbone. Other parameters differ by no more than 3σ between the phases and the root-mean-square (rms) fit of chemically equivalent non-H atoms in the two molecular structures is 0.072 Å (Figure S1a). An intramolecular H-bond, N1–H1A···N2, forms between the unprotonated nitrogen atom (N2) and the ammonium group. The geometry of this H-bond is the same in the two structures, with the distance between the donor and the acceptor nitrogen atoms being 2.772(3) and 2.770(3) Å in phases I and II, respectively, and the angles at the hydrogen atom being 143° in both polymorphs.

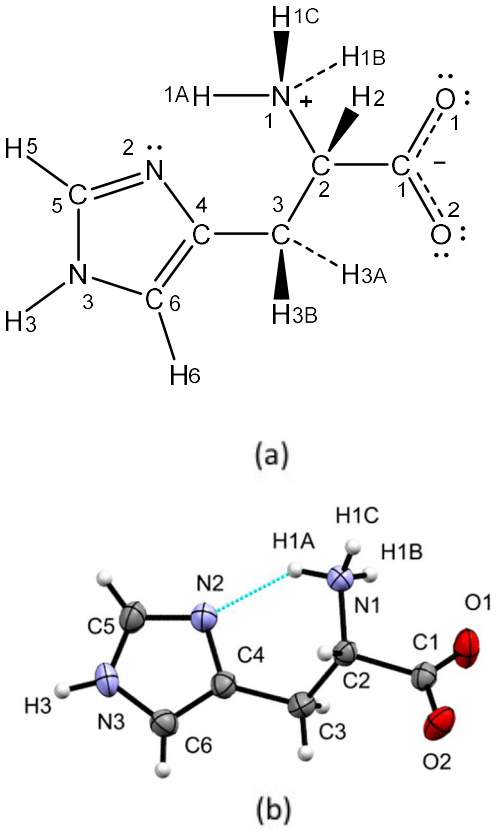

Figure 1. (a) Numbering scheme and connectivity in *L*-histidine. (b) Labelling of the H-atoms involved in the intermolecular H-bonds (shown for phase I). The intramolecular H-bond is shown as a blue dotted line.

At ambient conditions, the first molecular coordination sphere in both polymorphs contains 12 molecules in six symmetry-related pairs. The total energies of these contacts were calculated using the Pixel and SAPT methods. Since both calculations are sensitive to the H-atom positions, the energy values were computed using the DFT-optimised structures. A comparison between optimised and experimental structures is shown in Figure S1b-d in the ESI. Intermolecular interaction energies within the first molecular coordination spheres of the two polymorphs are listed in Tables 3 and 4, where they are grouped into symmetry-equivalent pairs labelled A/A', B/B' and so on. The molecule-molecule energies are broken down into their Coulombic, polarization, dispersion and repulsion terms.

Three conventional intermolecular H-bonds (described as contacts A, B and C in Figures 2 and 3) are formed by each molecule in both polymorphs, two originating from the ammonium group (N1) and the other formed by a nitrogen atom (N3) belonging to the imidazole ring. In all three cases, the acceptor is a carboxylate oxygen atom. Contact A involves N3–H3···O1 H-bonds, which form primary-level C(8) chains running along the *c*-direction (Figure 2).[66] In phase II the contact energy is –92.2 kJ mol^{-1} (DFT-optimised distance of H···O = 1.681 Å) and the molecules are related by lattice translations (Figure 2b). In phase I, the total energy is –99.0 kJ mol^{-1} (1.676 Å), but successive molecules in the chain are now related by a 2_1-screw operation so that the *c*-axis length is approximately double that in phase II (Figure 2a). In both polymorphs interaction B is mediated by N1–H1B···O2 H-bonds forming primary-level C(5) chains by lattice translations along the *a*-axis. These connect the chain formed along **c** to generate a layer of molecules in the *ac*-plane. The length and total molecule-molecule energy of the interaction in phases I and II are the same (1.801 Å and –33.9 kJ mol^{-1} in phase I and 1.789 Å and –34.1 kJ mol^{-1} in phase II). The layers in both phases are stacked along the *b*-axis via 2_1-

screw operations, where molecules form primary-level C(5) chains of N1–H1C···O2 H-bonds (Figure 3). These contacts (labelled C) are the most stabilising among all the intermolecular interactions, with the same total energy and length in the orthorhombic (–133.5 kJ mol^{-1}, 1.732 Å) and monoclinic (–133.6 kJ mol^{-1}, 1.707 Å) polymorphs.

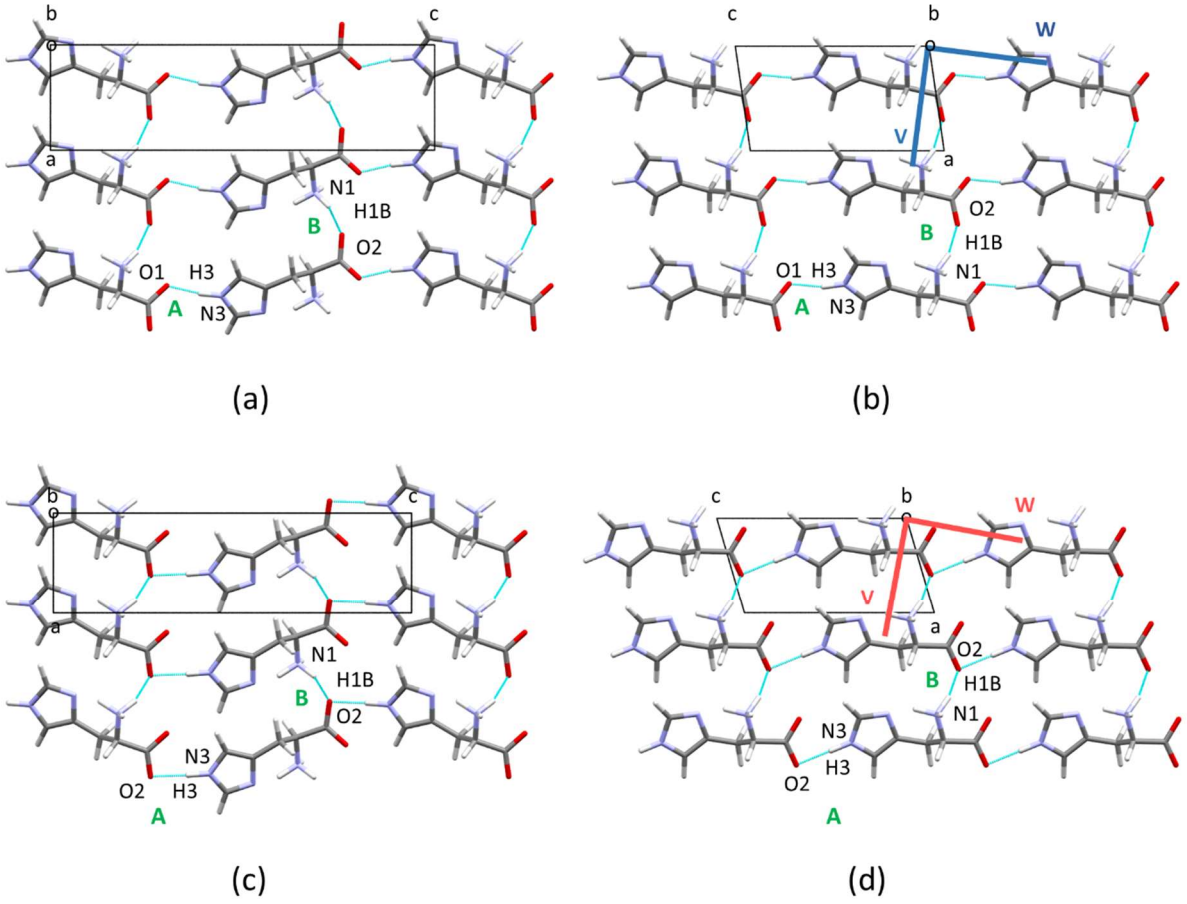

Figure 2. Hydrogen bonding in *L*-histidine at ambient pressure, as viewed along **b**, for phases I (a) and II (b). Hydrogen bonding in L-histidine at 6.60 and 6.85 GPa, also viewed along **b**, for phases I' (c) and II' (d), respectively. The principal directions of compressibility (**W** and **V**) before (blue) and after (red) the phase transition are shown for the monoclinic polymorph and centred at the origin of the unit cell. The third principal axis, **U**, lies along **b**. The contacts A and B referred to in the text and in Table 3, are labelled in green.

Table 1. Selected crystallographic information for the orthorhombic polymorph of *L*-histidine. Data collection performed at ambient temperature.

CCDC Deposition Number	**2020565**	**2020576**	**2020577**	**2020581**
Phase, Pressure (GPa)	**I, 0.00**	**I, 4.45**	**I', 4.62**	**I', 6.60**
Crystal data				
Crystal system, space group	Orthorhombic, $P2_12_12_1$	Orthorhombic, $P2_12_12_1$	Orthorhombic, $P2_12_12_1$	Orthorhombic, $P2_12_12_1$
a, b, c (Å)	5.1586 (5), 7.3367 (6), 18.7825(13)	4.8797 (5), 6.6367 (7), 18.251 (16)	4.8515 (5), 6.8861 (8), 17.238 (11)	4.7918 (3), 6.7777 (5), 17.040 (11)
α, β, γ (°)	90, 90, 90	90, 90, 90	90, 90, 90	90, 90, 90
V (Å^3), ρ (g/cm^3)	710.86 (10), 1.450	591.1 (5), 1.744	575.9 (4), 1.790	553.4 (4), 1.862
Radiation type	Mo $K\alpha$, λ = 0.71073 Å	Synchrotron, λ = 0.4859 Å	Synchrotron, λ= 0.4859 Å	Synchrotron, λ = 0.4859 Å
μ (mm^{-1})	0.11	0.07	0.07	0.07
Crystal size (mm)	0.35 × 0.30 × 0.15	0.25 × 0.15 × 0.15	0.25 × 0.25 × 0.15	0.25 × 0.15 × 0.15
Data collection				
Diffractometer	Agilent SuperNova	Beamline I19-EH2	Beamline I19-EH2	Beamline I19-EH2
Absorption correction	Multi-scan	Multi-scan	Multi-scan	Multi-scan
T_{min}, T_{max}	0.6816, 0.7454	0.6412, 0.7442	0.6056, 0.7442	0.6290, 0.7442
No. of measured, independent and observed [$I > 2\sigma(I)$] reflections	8266, 1440, 1251	1149, 448, 368	1092, 530, 428	728, 395, 325
R_{int}	0.045	0.024	0.036	0.025
θ_{mix}, θ_{max}(°), completeness	2.981, 25.242, 100%	2.232, 17.723, 38%	2.588, 17.694, 46%	3.653, 17.731, 36%
(sin $\theta/\lambda)_{max}$ (Å^{-1})	0.626	0.626	0.626	0.627
Refinement				
$R[F^2 > 2\sigma(F^2)]$, $wR(F^2)$, S	0.042, 0.069, 1.61	0.054, 0.108, 1.79	0.047, 0.097, 1.36	0.047, 0.099, 1.37
No. of unique reflections / parameters	1440 / 102	448 / 46	530 / 101	395 / 46
No. of restraints	0	25	100	25
$\Delta\rho_{max}$, $\Delta\rho_{min}$ (e Å^{-3})	0.20, −0.16	0.28, −0.23	0.19, −0.21	0.19, −0.18

Table 2. Selected crystallographic information for the monoclinic polymorph of *L*-histidine. Data collections performed at ambient temperature.

CCDC Deposition Number	**2020582**	**2020591**	**2020592**	**2020598**
Phase, Pressure (GPa)	**II, 0.00**	**II, 3.00**	**II', 3.21**	**II', 6.85**
Crystal data				
Crystal system, space group	Monoclinic, $P2_1$	Monoclinic, $P2_1$	Monoclinic, $P2_1$	Monoclinic, $P2_1$
a, b, c (Å)	5.1698 (4), 7.3884 (6), 9.4715 (7)	4.9324 (10), 6.7931 (13), 9.245 (4)	4.8807 (8), 6.7916 (11), 9.192 (3)	4.7210 (8), 6.7249 (10), 9.029 (14)
α, β, γ (°)	90, 98.177 (5), 90	90, 100.81 (3), 90	90, 103.38 (2), 90	90, 106.16 (4), 90
V (Å^3), ρ (g/cm^3)	358.10 (5), 1.439	304.28 (16), 1.694	296.44 (13), 1.738	275.3 (4), 275.3 (4), 1.872
Radiation type	Mo $K\alpha$, λ = 0.71073 Å	Ag $K\alpha$, λ = 0.56086 Å	Ag $K\alpha$, λ= 0.56086 Å	Synchrotron, λ = 0.4859 Å
μ (mm^{-1})	0.11	0.08	0.08	0.07
Crystal size (mm)	0.20 × 0.20 × 0.15	0.25 × 0.20 × 0.15	0.25 × 0.20 × 0.15	0.20 × 0.20 × 0.15
Data collection				
Diffractometer	Agilent SuperNova	Bruker D8 Venture	Bruker D8 Venture	Beamline I19-EH2
Absorption correction	Multi-scan	Multi-scan	Multi-scan	Multi-scan
T_{min}, T_{max}	0.5953, 0.7454	0.5972, 0.7445	0.4939, 0.7445	0.5850, 0.7442
No. of measured, independent and observed [$I > 2\sigma(I)$] reflections	3651, 1456, 1202	1421, 464, 340	1346, 410, 343	756, 382, 292
R_{int}	0.035	0.065	0.043	0.029
θ_{max}, θ_{max}(°), completeness	3.511, 26.378, 100%	3.318, 20.548, 38%	3.386, 20.537, 35%	3.044, 17.764, 34%
(sin $\theta/\lambda)_{max}$ (Å^{-1})	0.625	0.626	0.625	0.628
Refinement				
$R[F^2 > 2\sigma(F^2)]$, $wR(F^2)$, S	0.039, 0.067, 1.26	0.036, 0.069, 1.04	0.046, 0.098, 1.65	0.079, 0.164, 2.40
No. of unique reflections / parameters	1456 / 101	464 / 101	410 / 101	382 / 46
No. of restraints	0	100	100	25
$\Delta\rho_{max}$, $\Delta\rho_{min}$ (e Å^{-3})	0.20, −0.18	0.14, −0.13	0.21, −0.18	0.38, −0.35

In summary, of the four H-bond donors available in *L*-histidine, the ammonium-based H1A forms an internal H-bond, H1B and the imidazole-based H3 form the *ac*-layers, while H1C connects the layers along the *b*-axis. This description applies to both phases, and both are saturated in terms of H-bonding. Even though the symmetry operations which generate analogous H-bonds are different, the energies and lengths of the interactions are strikingly similar.

The H-bonded interactions account for three symmetry-related pairs within the first coordination sphere of each polymorph. Three further pairs of longer-range intermolecular interactions are also formed, all occurring between the *ac*-layers. The strongest of them connects the ammonium group and O1 (contact D in Figure 3), with a total energy of −58.5 kJ mol^{-1} and −55.4 kJ mol^{-1} in phases I and II, respectively. The interaction features three N1H1X···O1 contacts where X = A, B, C, with distances between 2.596 Å and 3.164 Å and <N1H1X···O1 between 75.52° and 106.35° in both phases. The distances are too long and the angles too tight for H-bonds, and they are better considered as

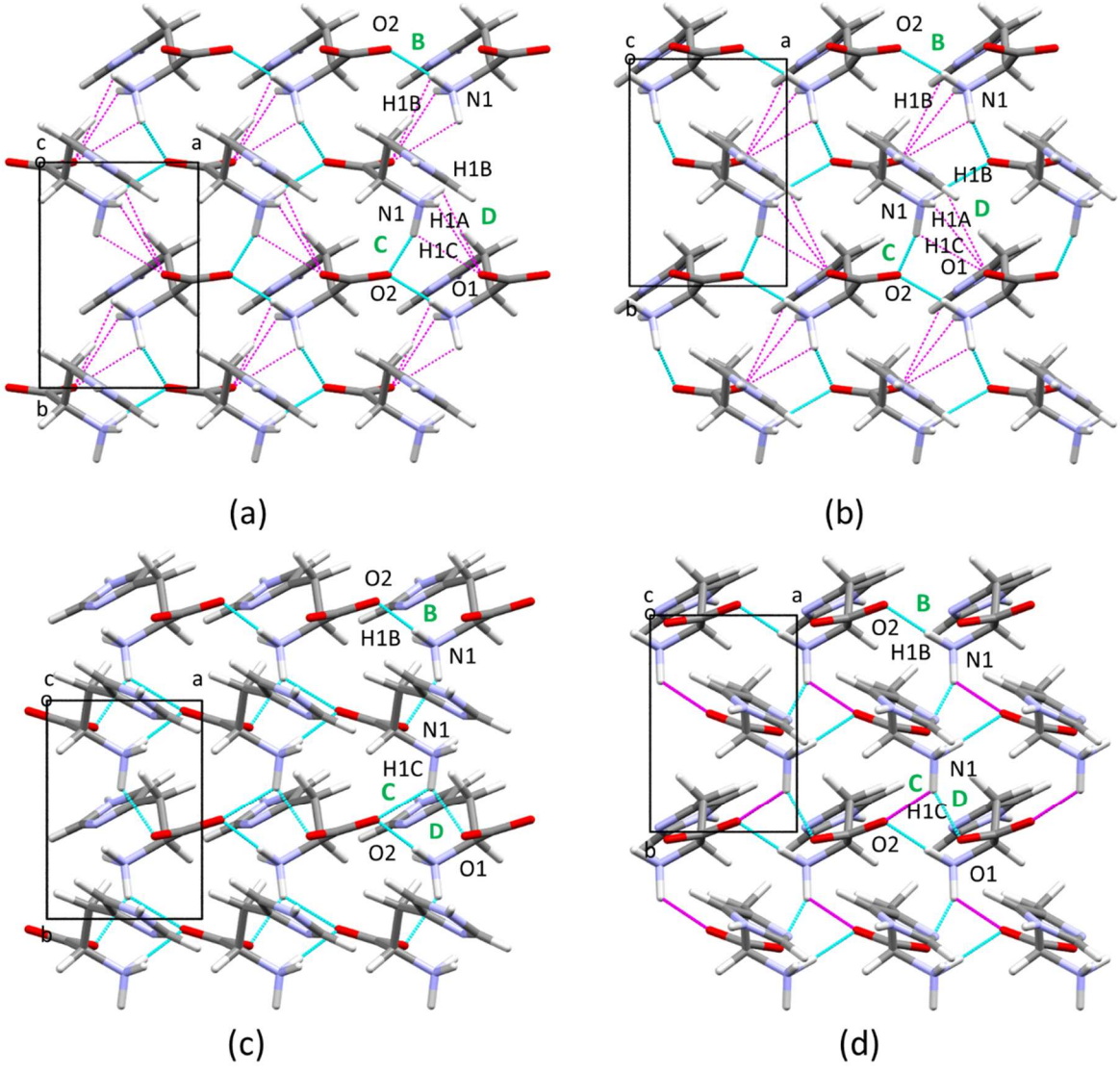

Figure 3. Hydrogen bonding (pale-blue) and electrostatic interactions (magenta) in *L*-histidine at ambient pressure, as viewed along **c**, for phases I (a) and II (b). With the same colour code, hydrogen bonding and electrostatic interactions in *L*-histidine at 6.60 and 6.85 GPa, as viewed along **c**, for phases I' (c) and II' (d), respectively. Contacts C and D are labelled in green. Parts (a) and (c) show only half of the unit-cell contents for the sake of clarity. The same views with the complete unit-cell contents are given in the ESI (Figure S3).

Table 3. Interactions in the first molecular coordination sphere of the orthorhombic polymorph of the amino acid *L*-histidine. All energies are in kJ mol^{-1}. Contact distances are to H-atom for DFT optimised structures.

Label	Symmetry	Pressure	Centroid Distance	Pixel / SAPT 2+3					Contact, direction
Phase I		(GPa)	(Å)	Coulombic	Polarisation	Dispersion	Repulsion	Total	(Å)
H-bonds									
A / A'	3/2 – x, 1 – y, – 1/2 + z 3/2 – x, 1 – y, + 1/2 + z	0.00	9.409	–116.7 / –110.2	–40.2 / –50.2	–12.7 / –25.4	70.6 / 94.8	–99.0 / –91.0	N3–H3···O1 = 1.676, along **c**
B / B'	– 1 + x, y, z 1 + x, y, z	0.00	5.159	–23.9 / –33.7	–35.8 / –39.9	–25.4 / –42.5	51.2 / 84.4	–33.9 / –31.7	N1–H1B···O2 = 1.801, along **a**
C / C'	1 – x, – 1/2 + y, 1/2 – z 1 – x, + 1/2 + y, 1/2 – z	0.00	7.071	–128.1 / –123.3	–47.5 / –55.9	–21.1 / –39.3	63.2 / 90.6	–133.5 / –128.0	N1–H1C···O2 = 1.732, along **b**
Electrostatic Interactions									
D / D'	2 – x, – 1/2 + y, 1/2 – z 2 – x, + 1/2 + y, 1/2 – z	0.00	6.811	–42.5 / –45.3	–11.8 / –10.8	–10.3 / –15.3	6.1 / 15.7	–58.5 / –55.8	N1H1X···O1 (X = A, B, C) = 2.596 - 3.133
E / E'	1/2 + x, 3/2 – y, 1– z – 1/2 + x, 3/2 – y, 1– z	0.00	6.372	–16.1 / –17.0	–6.8 / –6.3	–18.6 / –23.9	15.8 / 22.6	–25.7 / –24.6	C6H6···π_{ring} = 2.665
F / F'	– 1/2 + x, 1/2 – y, 1– z + 1/2 + x, 1/2 – y, 1– z	0.00	5.808	21.2 / 15.4	–7.1 / –5.7	–22.2 / –26.6	12.9 / 20.4	4.8 / 3.5	NH_3^+– NH_3^+ = 7.575, NH_3^+–ring = 5.033
Phase I'									
H-bonds									
A / A'	3/2 – x, 1 – y, – 1/2 + z 3/2 – x, 1 – y, + 1/2 + z	6.60	8.700	–127.6 / –127.3	–44.8 / –50.2	–20.9 / –35.1	75.5 / 109.1	–117.8 / –103.6	N3–H3···O2/O1 = 1.778 / 2.276, along **c**
B / B'	– 1 + x, y, z 1 + x, y, z	6.60	4.792	–35.0 / –58.5	–59.0 / –60.7	–48.6 / –75.1	132.3 / 186.7	–10.3 / –7.9	N1–H1B···O2 = 1.700, along **a**
C / C'	1 – x, – 1/2 + y, 1/2 – z 1 – x, + 1/2 + y, 1/2 – z	6.60	7.132	–94.2 / –97.0	–36.3 / –35.0	–22.0 / –39.3	36.1 / 63.5	–116.4 / –107.7	N1–H1C···O2 = 2.102, along **b**
D / D'	2 – x, – 1/2 + y, 1/2 – z 2 – x, + 1/2 + y, 1/2 – z	6.60	6.007	–112.2 / –122.5	–49.4 / –47.2	–31.8 / –50.2	87.3 / 117.7	–106.1 / –92.5	N1–H1C···O1 = 1.866, along **b**
Electrostatic interactions									
E / E'	2 – x, – 1/2 + y, 1/2 – z 2 – x, + 1/2 + y, 1/2 – z	6.60	6.076	–21.5 / –26.0	–14.3 / –11.4	–32.6 / –40.1	47.7 / 57.1	–20.7 / –20.5	C6H6···π_{ring} = 2.484
F / F'	– 1/2 + x, 1/2 – y, 1– z + 1/2 + x, 1/2 – y, 1– z	6.60	5.039	21.0 / 8.5	–18.7 / –12.4	–43.1 / –50.1	55.1 / 71.9	14.3 / 17.9	NH_3^+– NH_3^+ = 6.659, NH_3^+–ring = 4.517

Table 4. Interactions in the first molecular coordination sphere of the monoclinic polymorph of the amino acid *L*-histidine. All energies are in kJ mol^{-1}. Contact distances are to H-atom for DFT-optimised structures.

Label	Symmetry	Pressure	Centroid Distance	Pixel / SAPT 2+3					Contact, direction
Phase II		**(GPa)**	**(Å)**	**Coulombic**	**Polarisation**	**Dispersion**	**Repulsion**	**Total**	**(Å)**
	H-bonds								
A / A′	x, y, − 1 + z x, y, + 1 + z	0.00	9.472	−110.6 / −105.5	−39.4 / −49.9	−12.6 / −25.3	70.5 / 94.6	−92.2 / −86.1	N3−H3···O1 = 1.681, along **c**
B / B′	− 1 + x, y, z + 1 + x, y, z	0.00	5.170	−24.5 / −34.3	−35.8 / −39.9	−25.0 / −42.1	51.2 / 84.2	−34.1 / −32.1	N1−H1B···O2 = 1.789, along **a**
C / C′	1 − x, − 1/2 + y, 2 − z 1 − x, + 1/2 + y, 2 − z	0.00	7.092	−131.8 / −127.2	−49.9 / −59.7	−21.5 / −40.2	69.6 / 98.0	−133.6 / −129.1	N1−H1C···O2 = 1.707, along **b**
	Electrostatic Interactions								
D / D′	2 − x, + 1/2 + y, 2 − z 2 − x, − 1/2 + y, 2 − z	0.00	6.893	−40.4 / −42.0	−10.3 / −9.4	−8.9 / −13.3	4.2 / 11.8	−55.4 / −52.9	N1H1X···O1 (X = A, B, C) = 2.682 - 3.164
E / E′	1 − x, + 1/2 + y, 1 − z 1 − x, − 1/2 + y, 1 − z	0.00	5.675	−6.2 / −9.4	−8.0 / −7.1	−23.6 / −28.5	14.3 / 23.1	−23.5 / −21.8	C6H6···π_{ring} = 2.657
F / F′	2 − x, − 1/2 + y, 1 − z 2 − x, + 1/2 + y, 1 − z	0.00	6.584	8.7 / 6.0	−5.9 / -4.9	−16.8 / −21.7	13.4 / 18.7	−0.6 / −1.8	NH_3^+− NH_3^+ = 7.575, NH_3^+−ring = 4.969
	Phase II'								
	H-bonds								
A / A′	x, y, − 1 + z x, y, + 1 + z	6.85	9.029	−131.3 / −129.6	−46.2 / −49.8	−21.9 / −36.4	80.7 / 114.2	−118.7 / −101.7	N3−H3···O2/O1 = 1.785 / 2.221, along **c**
B / B′	− 1 + x, y, z + 1 + x, y, z	6.85	4.721	−31.2 / −55.6	−61.9 / −64.3	−48.0 / −74.8	134.9 / 188.8	−6.2 / −6.0	N1−H1B···O2 = 1.688, along **a**
D / D′	2 − x, + 1/2 + y, 2 − z 2 − x, − 1/2 + y, 2 − z	6.85	6.177	−124.5 / −132.5	−52.0 / −53.4	−30.8 / −50.3	97.1 / 137.0	−110.2 / −99.2	N1−H1C···O1 = 1.811, along **b**
	Electrostatic interactions								
C / C′	1 − x, − 1/2 + y, 2 − z 1 − x, + 1/2 + y, 2 − z	6.85	7.039	−90.9 / −94.9	−35.7 / −33.7	−22.5 / −39.9	36.0 / 63.5	−113.1 / −104.9	N1−H1C···O2 = 2.180
E / E′	1 − x, + 1/2 + y, 1 − z 1 − x, − 1/2 + y, 1 − z	6.85	5.052	−11.5 / −24.0	−24.6 / −17.0	−53.5 / −62.1	82.7 / 101.3	−6.9 / −1.8	C6H6···π_{ring} = 2.446
F / F′	2 − x, − 1/2 + y, 1 − z 2 − x, + 1/2 + y, 1 − z	6.85	6.153	8.3 / 3.2	−9.4 / -7.3	−24.4 / -30.6	25.2 / 33.6	−0.3 / −1.1	NH_3^+− NH_3^+ = 6.659, NH_3^+−ring = 3.464

electrostatic (or ionic) contacts. The remaining contacts consist of C6H6···π_{ring} (E) and C5H5···π_{ring} (F) interactions formed between imidazole rings in the layers (Figure S2 in the ESI). In phase I the C6H6···π_{ring} interaction stabilises the structure (–25.7 kJ mol^{-1}, 2.665 Å), while on the other side of the imidazole ring a destabilising interaction forms as positive regions of the electrostatic potentials of the contacting molecules approach each other (+4.8 kJ mol^{-1}, NH_3^+– NH_3^+, 7.575 Å, NH_3^+–ring, 5.033 Å). In phase II, the former contact is similar in energy (–23.5 kJ mol^{-1}, 2.657 Å) whereas the latter drops slightly to –0.6 kJ mol^{-1}, partly because the ammonium groups are further apart (NH_3^+– NH_3^+ 8.302 Å, NH_3^+–ring 4.969 Å).

3.2 The Effect of Pressure on the Unit-Cell Parameters

The variation of the unit-cell volumes and dimensions with pressure, normalised to their respective ambient-conditions parameters, is shown in Figure 4. The orthorhombic phase remains in the space group $P2_12_12_1$ from ambient pressure to 6.60 GPa but undergoes a single-crystal-to-single-crystal first-order phase transition at 4.5 GPa. Likewise, the monoclinic phase remains in the space group $P2_1$ from ambient pressure to 6.85 GPa undergoing a single-crystal-to-single-crystal first-order phase transition at 3.1 GPa. The crystal structures of both transformed polymorphs are similar in terms of symmetry and molecular positions and orientations to their parent phases and we shall refer to them as phases I' and II'.

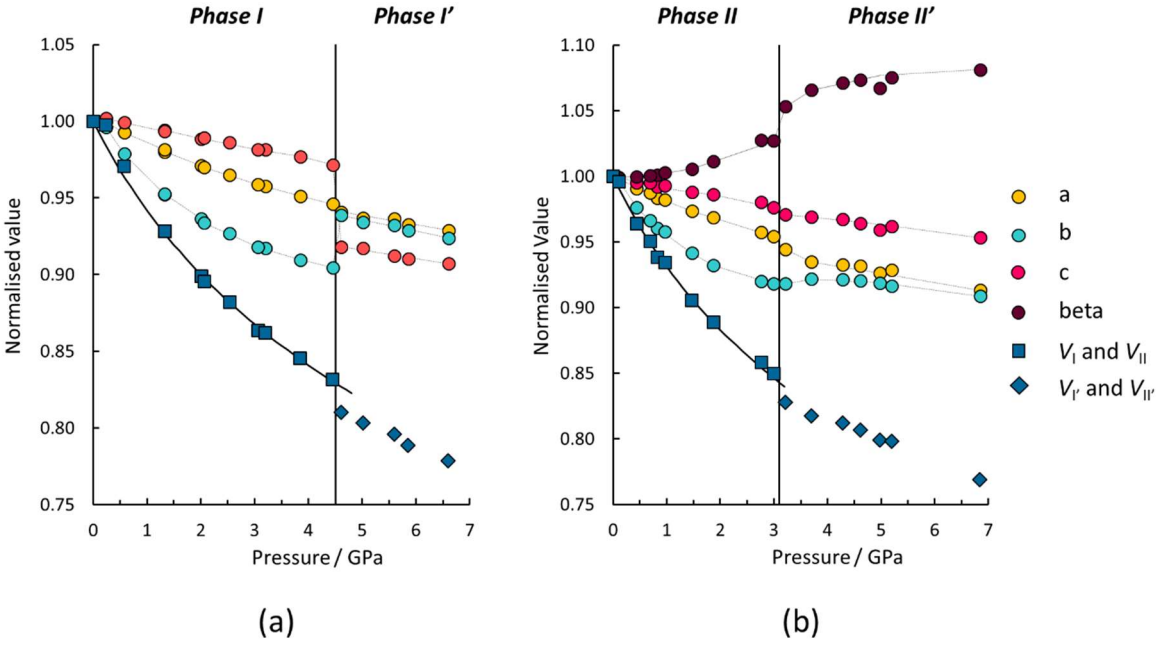

Figure 4. Variation of the normalised lattice parameters and unit-cell volume (*V*) of the orthorhombic (a) and monoclinic (b) polymorphs of *L*-histidine as a function of pressure. The black solid lines are the equations of state fitted to the volume data of phases I and II. Grey dashed lines are meant to guide the eye only.

Pressure-volume data of phases I and II were fitted to 3rd-order Birch-Murnaghan equations of state, with parameters shown in Table 5. The bulk moduli of phase I and II are 14.0(5) GPa and 11.6(6) GPa, respectively. These values are comparable to those of other amino acids. *e.g. L*-alanine (13.1(6) GPa) and *L*-threonine (15.23(8) GPa).[67,68] Despite the similarity in the intermolecular interactions, phase II is slightly, but significantly, softer than phase I, the difference reflecting the densities of the polymorphs at ambient conditions (1.450 and 1.439 g cm^{-3}, for phases I and II, respectively), as would

be expected. Prior to the phase transitions, the volume of phase I at 4.45 GPa is reduced by 16.9% compared to its ambient pressure value; in phase II, being softer, the volume is already reduced by a similar amount (15.0%) at 3.00 GPa (Figure 4). The volumes of phases I' and II' are well below those extrapolated from their parent phases.

Table 5. Parameters for the 3rd-order Birch-Murnaghan equations of state of phase I and II, at 298 K. For both polymorphs, V_0 was held fixed to its respective experimental value. The value of K'' is implied from the values of K_0 and K'.

	Phase I	**Phase II**
$\boldsymbol{T_0/K}$	298	298
$\boldsymbol{V_0/\text{Å}^3}$	710.86	358.10
$\boldsymbol{K_0/GPa}$	14.0(5)	11.6(6)
$\boldsymbol{K'}$	5.8(5)	5.2(7)
$\boldsymbol{K''/GPa^{-1}}$	–0.63615	–0.56689
$\boldsymbol{Reduced-\chi^2}$	1.26	1.29
$\boldsymbol{Maximum\ \Delta P\ /\ GPa}$	0.12	0.11

The unit-cell dimensions of both polymorphs respond in a similar way to pressure up to the phase transitions. The cell axes steadily decrease with *b* (9.5% in phase I at 4.45 GPa, 8.2% in phase II at 3.00 GPa) and *c* (2.8% in phase I, 2.4% in phase II) being the softest and hardest axes, respectively. In phase II, the β-angle increases gradually, causing sinβ to decrease by 0.77% (sinβ is relevant because $V = abc\sin\beta$ for a monoclinic unit cell).

Calculation of the strain tensors (using unit-cell dimensions at ambient pressure and before the phase transitions) confirms that the greatest compression occurs along the *b*-axis in both polymorphs. Paradoxically, this is the direction along which the strongest H-bond chain forms in both polymorphs (see Section 3.1). The second largest eigenvalue, labelled **V** in Figure 2, lies along **a** in phase I and makes an angle of 15° with the *a*-axis in phase II. Both directions are at least approximately perpendicular to the C(8) H-bonded chains formed along **c** (with **V** making an angle of 83° with the *c*-axis in phase II). The smallest eigenvalue, **W**, lies along these chains; the alignment is exact in phase I, while in phase II the angle between this direction and **c** is 7°.

The formation of phase I' and II' is marked by abrupt discontinuities in the unit-cell volume and dimensions. In the orthorhombic crystal, the volume decreases by 2.6% between 4.45 and 4.62 GPa. The *c*-axis, which had been the least compressible axis at lower pressures, abruptly shortens by 5.6%, while the *a*-axis decreases only by 0.6%. The *b*-axis, which had been the most compressible axis in phase I, lengthens by 3.6%. The compressibility becomes more isotropic in phase I', with the *a*, *b*, *c*-axes shortening by 1.2%, 1.7% and 1.1% respectively up to 6.60 GPa, preserving the order established of phase I. The unit cell volume of the monoclinic phase also reduces by 2.6% between 3.00 and 3.21 GPa. Although the volume difference is similar to that in the orthorhombic phase, the combined reduction of the axes only contributes ~60% of the volume reduction. The changes in the axis lengths are therefore more modest than in phase I and more uniform, with the magnitude of the decrease now following the order *a* (1.0%) > *c* (0.6%) > *b* (essentially no change). The decrease in sinβ is 1.0%,

a compression mechanism which would not be available in the orthorhombic phase I without a change in symmetry.

Beyond the phase transition, compressibility trends established in phase II change in phase II', with the order $b > a > c$ becoming a (shortening by 3.3% between 3.21 and 6.85 GPa) > c (1.8%) > b (1.0%). The b-axis increases by 0.4% between 3.21 and 4.28 GPa, with the trend reversing between 4.28 and 6.85 GPa. Sinβ declines by 1.27%. Analysis of the strain tensors indicates that the principal directions of compression between 3.21 and 6.85 GPa reorient, with **V** making an angle of 27° with **a** and **W** making an angle of 11° with **c** (Figure 2). Note that **b** is the least compressible axis in phase II', whereas it is the most compressible axis in phase I'.

The description of the intermolecular interactions in phases I and II in Section 3.1 was marked by the consistent similarity of the geometrical parameters and interaction energies. Nevertheless, the responses of the two phases to pressure are quite different.

3.3 The Effect of Pressure on the Intramolecular Interactions

The bond distances and angles were restrained to their ambient-pressure values during refinement of the high-pressure structures, and accordingly these parameters vary by no more than 3σ up to the highest pressure reached (Table S4-6). The application of restraints is justified by the root-mean-square deviations between the DFT-optimised and experimental molecular structures (Figure S1e-f along with further comments available in the ESI), which confirm the absence of pressure sensitivity in the primary intramolecular bond distances and angles. In both polymorphs, the largest conformational change occurs in the orientation of the carboxylate and ammonium groups (O2–C1–C2–N1, τ1, Figure 5).

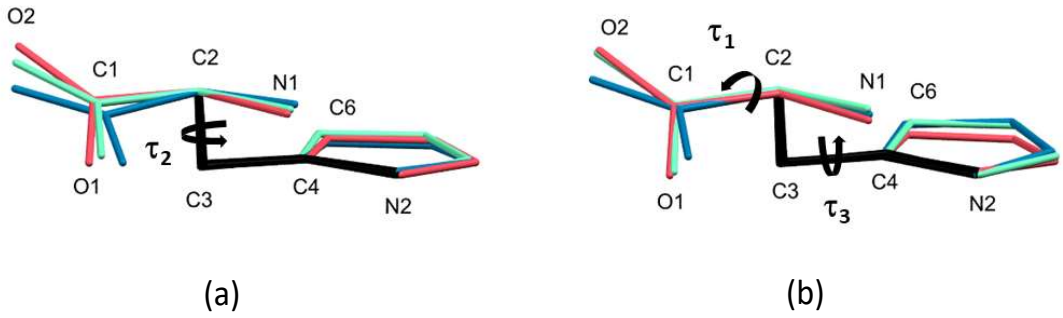

Figure 5. Structure overlay of the orthorhombic (a) and monoclinic (b) polymorphs of the amino acid *L*-histidine at ambient pressure (red), just below the phase transition (green) and at the highest pressure (blue). H atoms are omitted for clarity. Both sets of structures are overlaid along the C2–C3–C4–N2 torsional angle (represented in black) which shows the least sensitivity to pressure in both polymorphs (when the rigidity of the imidazole ring is excluded). The torsional angles analysed in the text are showed as black arrows and labelled.

In phase I and I', τ1 varies linearly with pressure (Figure 6), increasing from 155.02(19)° to 164.8(5)° between 0 and 6.60 GPa. By contrast, it hardly changes at all in phase II, before jumping abruptly from 155.2(6)° to 158.5(9)° at the transition to phase II'. The phase transition is marked in phase I by a sudden change in the orientation of the amino acid moiety and the imidazole side chain, represented by the torsion C1–C2–C3–C4 (τ2) which jumps from −177.5(6)° to −169.3(6)°. In addition, the orientation of the imidazole ring in phase II changes, with C2-C3-C4-C6 (τ3) declining from −127.8(3)° to −118.7(9)° below the phase transition, flattening off in phase II' and reaching −114.6(15) at 6.85 GPa (Figure S4 in the ESI).

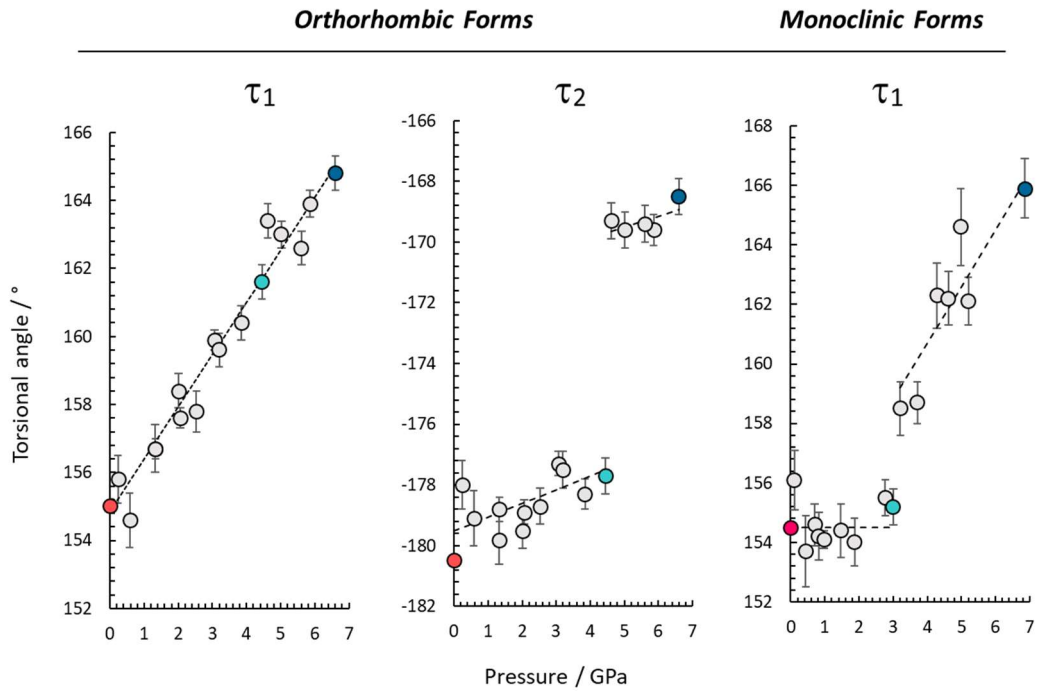

Figure 6. The torsion angles τ1 and τ2 as a function of pressure, in the two polymorphs of the amino acid *L*-histidine. The colour coding used is the same as Figure 5. Dashed trend lines were obtained through χ^2 minimisation.

3.4 The Effect of Pressure on the Intermolecular Interactions

The effects of pressure on the changes in lattice energy (ΔU) and enthalpy (ΔH) of the *L*-histidine polymorphs are shown in Figure 7, with the points calculated using periodic DFT. The lattice energy increases steadily under compression of both polymorphs (Figure 7a-b). At the phase transition, both exhibit a similar discontinuity, with the lattice energy being approximately 9 and 7 kJ mol^{-1} higher than that extrapolated for phases I and II, respectively, at the same pressures. Such a destabilisation of the lattice energy is compensated by the $P\Delta V$ contribution to the enthalpy change at the transition. This term accounts for −32.6 and −8.3 kJ mol^{-1} in the orthorhombic and monoclinic polymorphs, respectively, as calculated from the difference between the volumes of phases I and II extrapolated using the equation of state (587.65 and 300.76 Å^3) and the observed volumes of phases I' and II' (575.9 and 296.44 Å^3) immediately after the transitions at 4.62 and 3.21 GPa, respectively. The transitions are thus driven by the need to pack the molecules more efficiently at higher pressures. The

orthorhombic form shows a smooth trend in enthalpy change up to the highest pressure (Figure 7c), while in the monoclinic form there is a small discontinuity at the phase transition (Figure 7d).

Animations showing the compression mechanism of both phases of histidine are available in the ESI, while the energies of the six unique contacts formed in the first coordination sphere are shown in Figure 8 as a function of centroid-centroid distance. In the parent phases, the energies of contacts B, E and F become progressively more positive. Meanwhile, the total energies of contacts A and D decrease significantly with pressure, providing a thermodynamically favourable means to accommodate compression. Contact C is barely affected by the pressure increase in phase I (+0.6 kJ mol^{-1}), while it stabilises slightly in phase II (–6.3 kJ mol^{-1}). The combination of the trends leads to a *stabilisation* of the first molecular coordination sphere with pressure, meaning that in the early stage of compression the overall increase in lattice energy comes from longer-range electrostatic interactions. The first coordination sphere starts to destabilise in the new phases I' and II'.

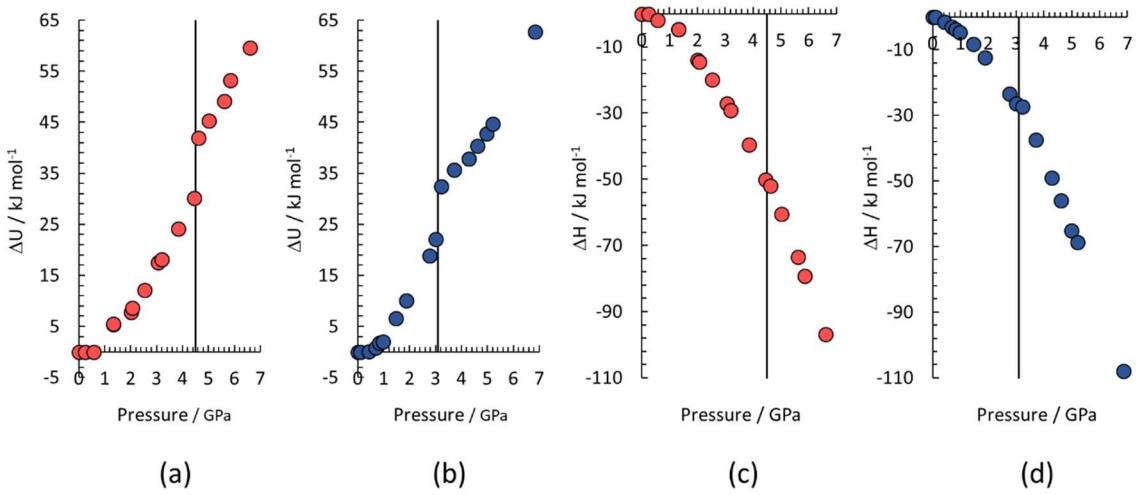

Figure 7. Variation of the lattice energy (a and b) and enthalpy (c and d) of the orthorhombic (red) and monoclinic (blue) polymorphs of *L*-histidine. The points are relative to ambient pressure. Vertical black lines highlight the phase transitions.

3.4.1 The Effect of Pressure on the Intermolecular Interactions within the *ac*-layers

The biggest energetic change within the *ac*-layers occurs in interaction A. The geometry of this contact changes in a similar way in phases I and II (Figure 9a). The N3–H3···O1 H-bond geometry becomes less favourable through the narrowing of the angle subtended at H3, while the other oxygen atom in the same molecule (N3–H3···O2) shortens its distance to H3. In phase I, the shortening of these contacts is accompanied by a rotation of the amino-acid moiety while in phase II a rotation occurs in the orientation of the imidazole ring (Figure 5).

In the orthorhombic polymorph, the acceptor atom in contact A swaps from O1 to O2 at the phase transition to phase I', so that N3–H3···O2 becomes the primary H-bond (Figure 9a). In the monoclinic polymorph the same contact initially becomes three-centred at the transition, the switch between oxygen atoms occurring just after the formation of phase II'. A longer-range C6H6···O1 contact also

forms in both phases. These rearranged H-bonds drop the total energy of contact A to similar values of −117.2 kJ mol^{-1} in phase I' at 4.62 GPa, and −119.1 mol^{-1} in phase II' at 3.71 GPa. Nevertheless, the reduction of the centroid-centroid distance in the phase I to I' transition is much greater (0.39 Å) than

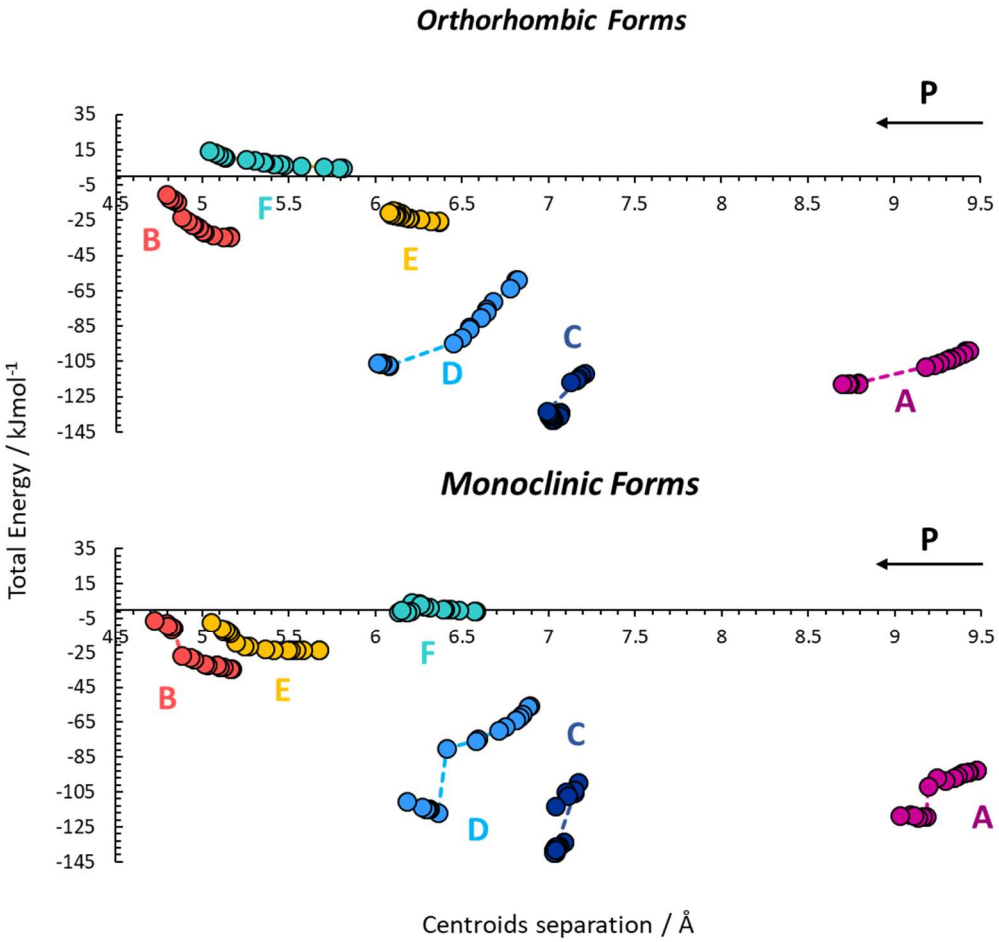

Figure 8. Intermolecular interaction energies calculated using the Pixel method for contact A-F as a function of centroids separation. For all the contacts, except C, the centroid-centroid distance decreases with pressure (*P*) going from the right side to the left (shown as black arrow). At the phase transitions, pressure goes in the opposite sense for contact C, going from the left side to the right as the contact increases in length.

in the II to II' transition (0.05 Å) so that the discontinuity in the *c*-axis length is much more marked in the former (Figure 4). In the new phases, the geometries of the H-bonds and the total energies of contact A remain essentially unchanged up to the highest pressures (Figure 2).

The H-bond distance in contact B (N1−H1B···O2) sees the largest shortening amongst the conventional H-bonds with pressure in phase I and II. By contrast with contact A, this leads to a destabilisation in the interaction energy as the result of like-charged moieties being pushed into closer proximity. At the transitions into phases I' and II' the H-bond distances lengthen abruptly, although the centroid-centroid distances drop by 0.03 Å and 0.05 Å, respectively. The <N1H1B···O2 angle narrows smoothly in the former polymorph, but drops by 9° in the latter (Figure 9b). The shortening that occurs in phases I' and II' with pressure is much reduced by comparison with phases I and II, while the energy steadily increases.

3.4.2 The Effect of Pressure on the Intermolecular Interactions between the *ac*-layers

The largest stabilisation with pressure occurs in the electrostatic contact D, which is formed between the *ac*-layers. This contact is characterised by much greater flexibility than the more directional H-bonds. In phase I, the energy of the interaction stabilises by 36 kJ mol^{-1} with a reduction in centroid-centroid distance of 0.36 Å; the corresponding figures for phase II are 24.8 kJ mol^{-1} and 0.48 Å. Such a favourable response to compression explains why, in both polymorphs, **b** is the softest of the three crystallographic axes. In phase I (Figure 9c), the oxygen and hydrogen atoms involved in N1H1X···O1 approach one another, increasing the <N1H1C···O1 angle (X = A, B and C). Conversely, in phase II only the O1···H1C distance changes, while the angle subtended at H1C remains constant. This is due to the τ1 torsion (Figure 5), which does not vary until the transition to phase II' occurs.

Contact C, which involves the N1H1C···O2 H-bond, plays a lesser role in the responses of both phases prior to the phase transitions in terms of both distance and energy (Figure 8). The H1C···O2 distance in phase I begins to increase with pressure above 2 GPa but is quite insensitive in phase II. The <N1H1C···O2 angles, both become less linear; as for contact D, the effect is more marked in phase I.

At the phase transition to phase I', contacts C and D transform into a three-centred N1H1C···O1/O2 H-bond. In phase II', the two interactions swap their character, contact D becoming an H-bond and contact C becoming more akin to a long-range electrostatic contact. The total energy of contact D drops by 12.6 kJ mol^{-1} between 4.45 and 4.62 GPa and by 8.2 kJ mol^{-1} between 3.00 and 3.71 GPa, in phase I' and II' respectively. In the same pressure ranges, interaction C becomes less stable, with its total energy increasing by 21.1 kJ mol^{-1} and by 38.8 kJ mol^{-1}, in phases I' and II' respectively. In the new phases, contact C and D shorten in a similar way up to the highest pressure (Figure 3). However, while contact C decreases the total energy, contact D becomes less stable.

The discontinuity of the *b*-axis seen in the orthorhombic polymorph at the phase transition (Figure 4) is less related to the behaviour of the intermolecular interactions C and D, than to the abrupt change of the intramolecular torsion τ2 (Figure 5). Such behaviour of the *b*-axis is not seen in the monoclinic polymorph, as τ2 barely changes across the transition to phase II' (from −177.8(8)° to −176.3 (15)°). The different structural change between the polymorphs is related to the different symmetry operators involved in the *ac*-layer. The animations of the pressure series show that, in the monoclinic polymorph, the lack of the 2_1-screw operation along the *c*-direction enables neighbouring rows of molecules linked by N3H3···O1 (O2 in phase II') to shear, allowing them to pack efficiently at the transition. In the absence of a symmetry-lowering phase transition, this degree of freedom is absent in the orthorhombic polymorph, where the molecules are constrained by 2_1-screw operations along both the **a** and **c** directions. Therefore, the transition occurs by the intramolecular torsion τ2, which twists the molecules toward the *b*-axis, enabling them to approach more closely in the *ac*-layer.

Minor structural differences between the two polymorphs are also seen in the other contacts involved in the molecular first-coordination sphere. Contact E and F destabilise in both polymorphs up to the phase transition (Figure 8), continuing the trend in phase I'. In phase II', the former continue to become less negative while the latter remains energetically constant. Along the pressure series, interaction E shortens ~50% more in the monoclinic form than in the orthorhombic form, while the opposite behaviour is seen for contact F.

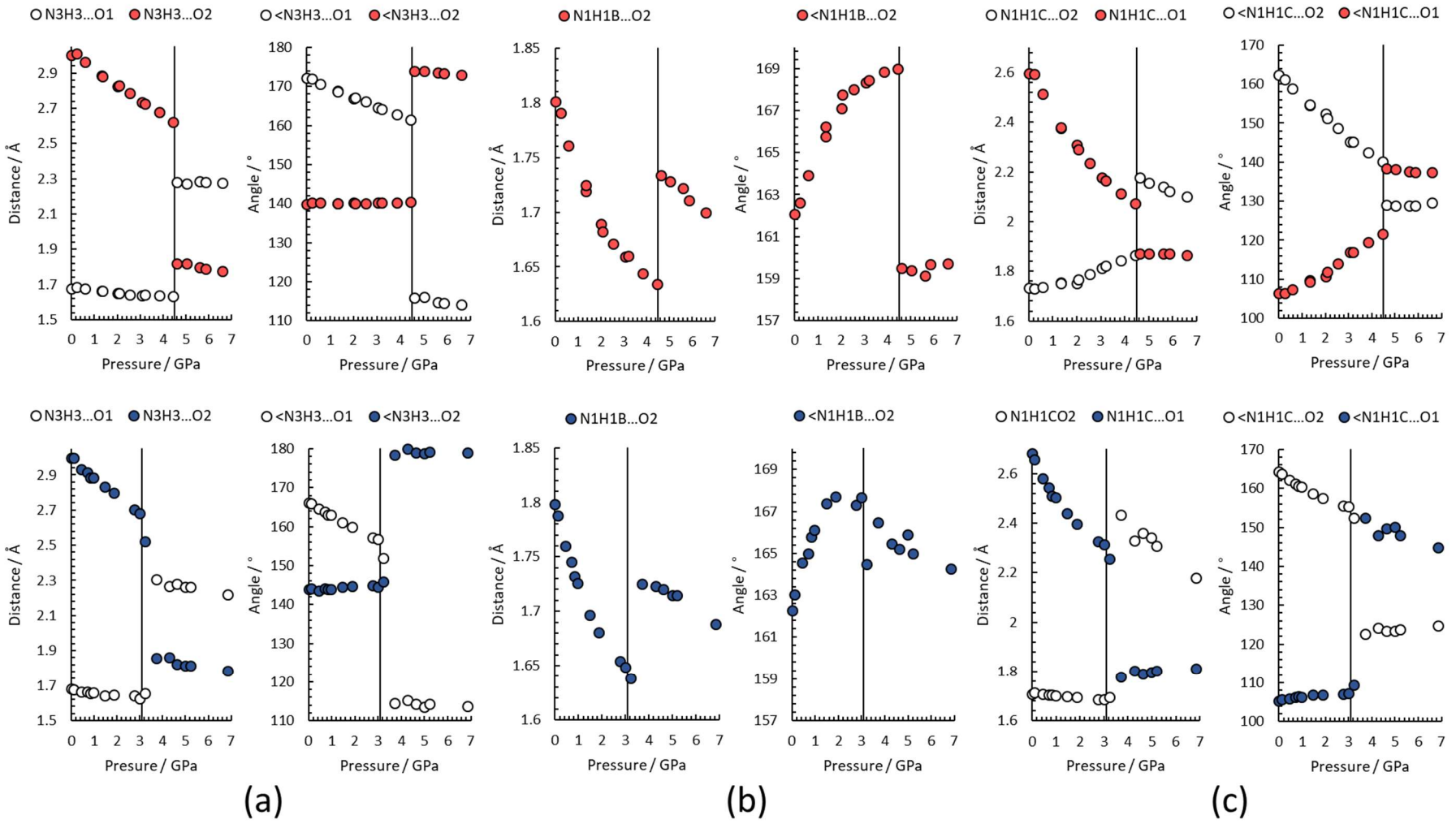

Figure 9. Donor-acceptor distances and angles of the H-bonds involved in contact A (**a**), B (**b**), C and D (**c**) for the orthorhombic (upper graphs) and monoclinic (lower graphs) polymorphs of *L*-histidine. Geometries are taken from the DFT-optimised structures. The vertical lines highlight the phase transitions.

3.5. Volume Relationships

The responses of the crystal structures of the two polymorphs of histidine to pressure consist of a combination of intra- and inter-molecular effects, the phase transitions being driven by minimisation of volume. The relative contributions made by the bonds, contacts and void space to volume reduction was analysed using a Monte Carlo procedure in which the volumes enclosed by the molecules and network of intermolecular contacts are identified as lying within the van der Waals radius of any atom.

The effect of the changes in molecular conformation on the molecular volume (V_{mol}) are shown in Figure 10a-b; the molecules have a volume of about 141 Å^3 in both phases. Prior to the phase transitions the histidine molecule is less compressible in phase I, with a 'molecular' bulk modulus (calculated from the molecular-volume-versus-pressure data) of 642(12) GPa, compared to 513(20) GPa in the monoclinic phase. Both phases experience a discontinuous drop at their phase transitions, but otherwise the variation of volume with pressure is quite linear. The high values of the bulk moduli, which are of a similar order of magnitude to diamond (445 GPa), reflect the incompressibility of covalent bonds and angles, and the compression that does occur is the result of torsional changes.

The volume of the network (V_{net}) of contacts formed within the van der Waals of the atoms is slightly smaller than ZV_{mol} because the van der Waals surfaces of the molecules overlap. In the orthorhombic phases the network volume per molecule is 115.52(8) Å^3 at ambient pressure, dropping to 113.37(5) Å^3 at 6.60 GPa. The network in the monoclinic phases is softer, corresponding data being 112.44(7) Å^3 at ambient pressure and 106.05(4) Å^3 at 6.85 GPa. In phase I, V_{net} decreases sharply up to 1 GPa, but then flattens off between 1 and 3 GPa, only to drop again immediately before the phase transition (Figure 10c). The matching discontinuities in the void volume, which must be present, are hardly discernible in Figure 10d because they are overwhelmed by the greater overall compressibility of the voids. At the I to I' transition the volume then *increases* sharply by 3 Å^3 per molecule, the expansion being compensated by a larger drop in the void volume (6.8 Å^3 per molecule).

Phase II shows a smoother trend in V_{net} up to 2.77 GPa, but then, as in phase I, it begins to drop immediately before the transition (Figure 10e). Here too, the volume then increases (by 1.1 Å^3 per molecule), but by a smaller amount than at the I to I' transition. It is also notable that this change occurs just after the II to II' transition, not at the transition itself. By contrast, a drop in the void volume of 3 Å^3 per molecule occurs at the transition (Figure 10f). The mismatch between the discontinuities in V_{net} and V_{void} is unexpected but was also noted in the context of the initial bifurcation between O1 and O2 of the H bond formed by the imidazole based H3 at the phase transition, followed by a complete swap from O1 to O2 just afterwards (Figure 10a).

The contributions from the networks and voids to the overall bulk moduli quoted in table 5 are given by

$$\frac{V}{K} = \frac{V_{net}}{K_{net}} + \frac{V_{void}}{K_{void}} \qquad [1]$$

Where K is the overall bulk modulus, V is the unit cell volume, K_{net} the bulk modulus of the network and so on (see ESI).

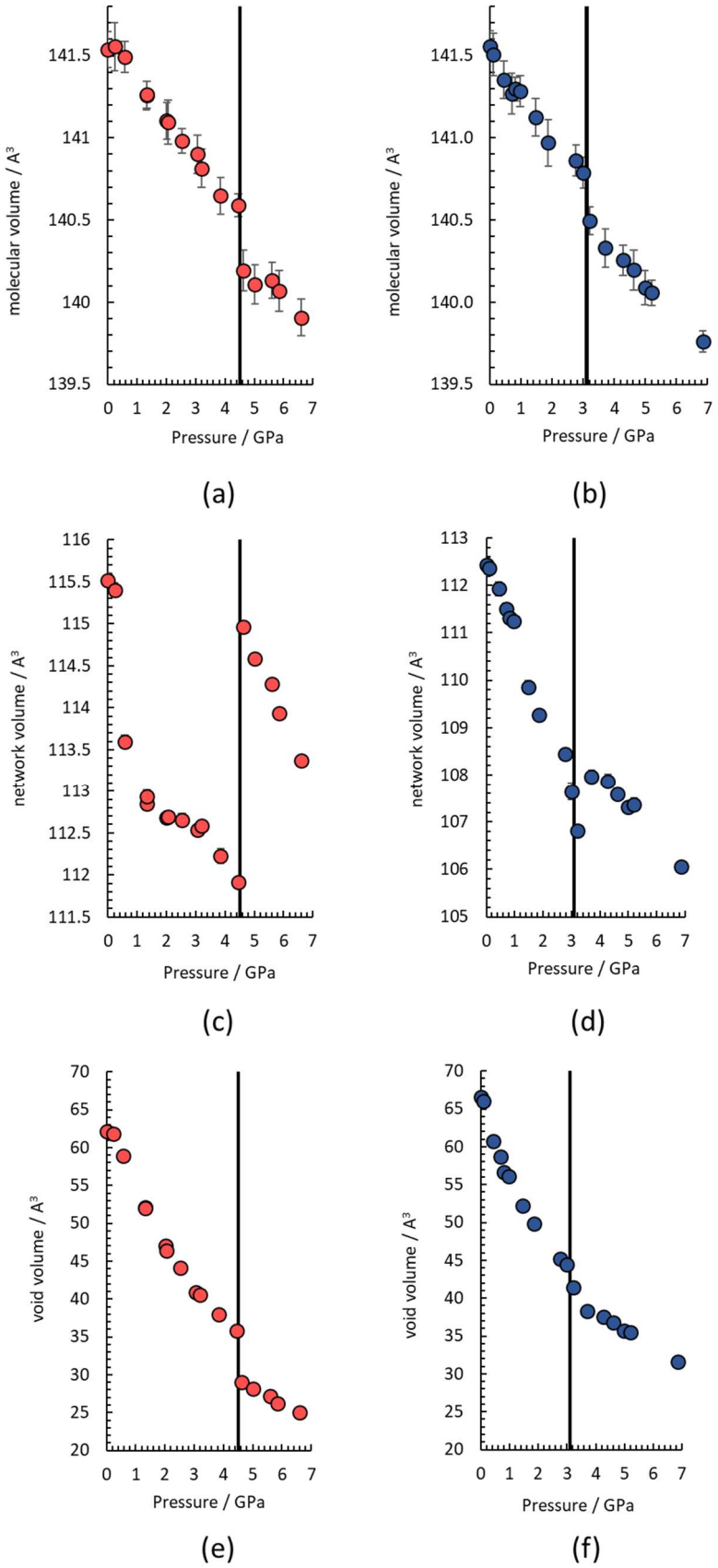

Figure 10. The effect of pressure on the molecular volume (V_{mol}; a, b), network volume (V_{net}; c, e), and void volume (V_{void}; d, f), for the orthorhombic (red) and monoclinic (Blue) polymorphs of *L*-histidine. Volume calculations were performed on the DFT-optimised structures.

The bulk modulus of the phase II network is 67(2) GPa, while those of the voids in phases I and II are 5.3(3) and 4.29(15) GPa, respectively. These values were determined from second- (network) and third- (voids) order Birch-Murnaghan equations of state (Table S8 in the ESI). They should be regarded as approximate as the fits are quite rough (see Figure S5 in the ESI). This comment applies particularly to the fit of the network volume in phase II. Indeed, the corresponding data for phase I could not be fitted at all, as would be expected from the form of Figure 10c, which shows very high compression at low pressure followed by the rapid onset of a much less compressible regime. While it is possible to estimate K_{net} in phase I to be 115 GPa from Equ. 1, the value is extremely sensitive to small variations in the values of the other parameters. Instead, an estimate of the average value of K_{net} in phase I between 0 and 4.45 GPa can be obtained from

$$K = \frac{V_f + V_0}{2} \frac{P_f + P_0}{V_f - V_0} \qquad [2]$$

Where the subscript '0' refers to ambient conditions, while '*f*' refers to the highest pressure reached in phase I (4.45 GPa), giving a value of 140 GPa. The values of K_{net} (phase II) = 69 GPa and K_{void} = 8.3 (phase I) and 7.5 (Phase II) GPa calculated from Equ. 1 are not very different to the values obtained from the equation-of-state fitting.

From this it is concluded that the higher overall bulk modulus seen for phase I (14.0(5) versus 11.6(6) GPa for phase II) reflects a greater resistance to compression in the molecules themselves, in the network of contacts and in the void spaces, but Equ. 1 shows that it is the last of these that is most important. The overall bulk moduli are much lower than the network moduli as a result of the reciprocal dependence on *K*, which makes soft components more influential than hard components.

4. Conclusions

The crystal structures of the orthorhombic and monoclinic polymorphs of the amino acid L-histidine have been determined by single-crystal X-ray diffraction up to 6.60 GPa and 6.85 GPa, respectively. Isosymmetrical single-crystal-to-single-crystal first-order phase transitions were observed at 4.5 GPa and 3.1 GPa for the orthorhombic and monoclinic polymorphs, respectively. Analysis of the changes in lattice energy and enthalpy indicates that the transitions undertaken by the polymorphs are driven by the need to pack the molecules efficiently at high pressures, thereby minimising the Gibbs free energy via the contribution of the pressure × volume (*PV*) term.

At ambient conditions, the molecular conformation, the intermolecular interaction energies and the crystal packing are strikingly similar in the two polymorphs. Indeed, the description of the H-bonds and their energies in the two phases presented in Section 3.1 almost reads like a crystallographic Spot-the-Difference competition. Nevertheless, their responses to pressure were found to be quite different. Phase II is softer than phase I, with a bulk modulus of 11.6(6) GPa compared to 14.0(5) GPa, respectively. The difference persists to the separate components of the structures, the molecules, the network formed by the intermolecular contacts and the void spaces, which are all softer in phase II.

The order of compressibility follows the densities of the polymorphs at ambient conditions, as would be expected. However, the symmetry operators involved in assembling the crystal structures of phase

I and II are also different. The lack of the 2_1-screw operation along the *c*-direction in phase II enables neighbouring rows of molecules linked by N3H3···O1 to shear, which causes a gradual decrease in sinβ. The same effect results in a ~40% contribution in volume reduction at the transition to phase II'. This compression mechanism cannot occur in the orthorhombic polymorph, where the molecules are constrained by 2_1-screw operations along both the *a*- and *c*-directions. The monoclinic polymorph therefore has more degrees of freedom available to it in its response to pressure, and we suggest that this also contributes to the relative softness of the monoclinic form.

Phase stability is determined by inter- and intra-molecular energies, volume and entropy, not symmetry, and so the idea that symmetry controls the compression of intermolecular contacts can be criticised from a thermodynamic viewpoint. A structure would be expected to undergo a phase transition in order to minimise its free energy as pressure increases. However, there will usually be a kinetic barrier to a transition which involves a substantial structural rearrangement, and many published high-pressure crystal structures may well be metastable forms which are 'trapped' by kinetics. Symmetry therefore plays a role because it determines the number of degrees of freedom that are available for accommodating pressure.

Some support for the suggestion that low symmetry may enhance compressibility can be found is other materials. Data on polymorphs of organic materials are quite sparse (Table S1), but work on paracetamol suggests that the monoclinic form is very slightly more compressible than the orthorhombic form, while for glycine the trigonal γ polymorph has a bulk modulus of 23.2(9) GPa,[69] whereas that of the monoclinic α form has been measured to be 14.8(20) GPa in one study and 19.5(7) GPa in another.[22,23] However, discordant results were obtained for the monoclinic and orthorhombic polymorphs of 2,4,6-trinitrotoluene (TNT). Although the bulk moduli are not statistically different (m-TNT K_0= 8.53(12) GPa and o-TNT K_0= 7.3(3) GPa), the values suggest that the low-symmetry monoclinic form is less compressible.[70]

More data are available by spreading the net beyond organic solids. Neutron powder diffraction experiments performed on the monoclinic polymorph of phosphoric acid showed that it converts to a more efficiently packed, and thus harder, orthorhombic phase during pressure release at 1.97 GPa; the bulk moduli being 13.81(15) and 17.61(36) GPa, respectively, following the expected trend.[71] A similar study performed on the orthorhombic form of $Sc_2W_3O_{12}$ showed that it undergoes a phase transition between 0.25 and 0.3 GPa to a softer monoclinic phase, with bulk moduli respectively of 32(2) and 11.8(8) GPa.[72] A Raman and synchrotron X-ray diffraction study on three polymorphs of alane, AlH_3,(orthorhombic γ, trigonal α, cubic β) found their bulk moduli to be 42(2), 45(3) and 58(4) GPa, respectively.[73] The trigonal α, hexagonal β and the high-pressure cubic γ- phases of the semiconductor silicon-nitride (Si_3N_4) have bulk moduli of 248, 256 and 300 GPa, respectively.[74] The three polymorphs of Mg_2SiO_4, which are the cubic ringwoodite γ, the orthorhombic olivine α and orthorhombic wadsleyite β, have bulk moduli of 181(3), 127.4(5) and 170(2) GPa.[75]

The present work has also investigated the decomposition of the overall volume changes in histidine into contributions from the network formed by intermolecular contacts and interstitial void space, which shows some interesting and unexpected trends. Both polymorphs exhibit premonitory drops in the volume of the network immediately prior to the phase transitions, but it is hardly discernible in the lattice energy plots of Figure 7. At the transitions themselves the network volume actually

increases. This effect is somewhat akin to negative linear compressibility, the increase of magnitude of certain lattice vectors with pressure.[76]

The values of the network bulk moduli seem, to us, surprisingly high [140 and 67 GPa for phases I and II, respectively]. They are similar to the overall values seen for harder ionic salts [e.g. CaF_2 82.0(7) GPa] and even moderately hard metals such as Sc (57 GPa) and Ti (110 GPa).[77,78] These data, along with the reciprocal contributions of component bulk moduli seen in Equ. 1 suggest that the softness of hydrogen-bonded molecular solids is due to the void space they contain rather than to the deformability of the H-bonds. It will be interesting to determine whether the same conclusion applies to other molecular solids.

5. Acknowledgements

We thank Professor Carole A. Morrison (The University of Edinburgh) for useful discussions and assistance with DFT calculations. We thank the Australian Nuclear Science and Technology Organisation (ANSTO, Australia), the Engineering and Physical Sciences Research Council (EPSRC, UK) and the University of Edinburgh for studentship funding to GN. We also thank Diamond Light Source for the allocation of beamtime (MT16139) and EPSRC for provision of equipment (grant number EP/R042845/1). This work has made use of the resources provided by the Edinburgh Compute and Data Facility (ECDF) (<http://www.ecdf.ed.ac.uk/>). Finally, we would like to thank the referees of this paper for their insightful comments.

6. Supporting Information

The Supporting Information is available free of charge at [Editors to insert DIO link]

The ESI contains Tables containing crystallographic details of high-pressure behaviour of polymorphs, crystallographic information for all structures, comparisons of intermolecular energies calculated using PIXEL and SAPT, bond distances, angles and torsions and equation of state data for the molecule, network of contacts and void space. Supplementary Figures show the comparison between optimised and experimental structures, intermolecular interactions involving imidazole rings, a more complete view of Fig. 3 and a plot of the variation of τ_3 with pressure in the monoclinic polymorphs. Additional notes on the variation of primary bond distances with pressure between 0 and 10 GPa and a derivation of Equ. 1. Movies depicting the effect of pressure on the crystal structures, including the phase transitions, are also included as separate gif animation files. Crystal, refinement and intensity data for all the structures collected in this work are available from the Cambridge Crystallographic Data Centre, quoting deposition numbers 2020565-2020598.

7. References

(1) Katrusiak, A.; McMillan, P. *High-Pressure Crystallography;* Springer Netherlands: Dordrecht, NL, **2004**.

(2) Fabbiani, F. P. A.; Pulham, C. R. High-pressure studies of pharmaceutical compounds and energetic materials. *Chem. Soc. Rev.* **2006**, *35*, 932-942.

(3) Boldyreva, E. V. High-pressure diffraction studies of molecular organic solids. A personal view. *Acta Crystallogr. Sect. A: Found. Crystallogr.* **2008**, *64*, 218-231.

(4) Lee, R.; Howard, J. A. K.; Probert, M. R.; Steed, J. W. Structure of organic solids at low temperature and high pressure. *Chem. Soc. Rev.* **2014**, *43*, 4300-4311.
(5) Boldyreva, E. V. Multicomponent organic crystals at high pressure. *Zeitschrift fur Krist.* **2014**, *229*, 236-245.
(6) McKellar, S. C.; Moggach, S. A. Structural studies of metal-organic frameworks under high pressure. *Acta Crystallogr. Sect. B Struct. Sci. Cryst. Eng. Mater.* **2015**, *71*, 587-607.
(7) Görbitz, C. H. Crystal structures of amino acids: From bond length in glycine to metal complexes and high-pressure polymorphs. *Crystallogr. Rev.* **2015**, *21*, 160-212.
(8) Oswald, I. D. H.; Beavers, C. M. The effect of extreme conditions on molecular solids. *CrystEngComm* **2019**, *21*, 4420-4421.
(9) Katrusiak, A. Lab in a DAC - high-pressure crystal chemistry in a diamond-anvil cell. *Acta Crystallogr. Sect. B: Struct. Sci. Cryst. Eng. Mat.* **2019**, *75*, 918-926.
(10) Guerain, M. A. A review of high pressure experiments for study of crystallographic behavior and polymorphism of pharmaceutical materials. *J. Pharm. Sci.* **2020**, *109*, 2640-2653.
(11) Boldyreva, E. V; Shakhtshneider, T. P.; Ahsbahs, H.; Sowa, H.; Uchtmann, H. Effect of high pressure on the polymorphs of paracetamol. *J. Therm. Anal. Calorim.* **2002**, *68*, 437-452.
(12) Yu, L.; Stephenson, G. A.; Mitchell, C. A.; Bunnell, C. A.; Snorek, S. V.; Bowyer, J. J.; Borchardt, T. B.; Stowell, J. G.; Byrn, S. R. Thermochemistry and conformational polymorphism of a hexamorphic crystal system. *J. Am. Chem. Soc.* **2000**, *122*, 585-591.
(13) Gushurst, K. S.; Nyman, J.; Boerrigter, S. X. M. The PO13 crystal structure of ROY. *CrystEngComm* **2019**, *21*, 1363-1368.
(14) Harty, E. L.; Ha, A. R.; Warren, M. R.; Thompson, A. L.; Allan, D. R.; Goodwin, A. L.; Funnell, N. P. Reversible piezochromism in a molecular wine-rack. *Chem. Commun.* **2015**, *51*, 10608-10611.
(15) Funnell, N. P.; Bull, C. L.; Ridley, C. J.; Capelli, S. Structural behaviour of OP-ROY at extreme conditions. *CrystEngComm* **2019**, *21*, 4473-4483.
(16) Fedorov, A. Y.; Rychkov, D. A.; Losev, E. A.; Zakharov, B. A.; Stare, J.; Boldyreva, E. V. Effect of pressure on two polymorphs of tolazamide: Why no interconversion ? *CrystEngComm* **2017**, *19*, 2243-2252.
(17) Tan, X.; Wang, K.; Li, S.; Yuan, H.; Yan, T.; Liu, J.; Yang, K.; Liu, B.; Zou, G.; Zou, B. Exploration of the pyrazinamide polymorphism at high pressure. *J. Phys. Chem. B* **2012**, *116*, 14441-14450.
(18) Hunter, S.; Coster, P. L.; Davidson, A. J.; Millar, D. I. A.; Parker, S. F.; Marshall, W. G.; Smith, R. I.; Morrison, C. A.; Pulham, C. R. High-pressure experimental and DFT-D structural studies of the energetic material FOX-7. *J. Phys. Chem. C* **2015**, *119*, 2322-2334.
(19) Dreger, Z. A.; Stash, A. I.; Yu, Z. G.; Chen, Y. S.; Tao, Y.; Gupta, Y. M. High-pressure structural response of an insensitive energetic crystal: 1,1-Diamino-2,2-dinitroethene (FOX-7). *J. Phys. Chem. C* **2016**, *120*, 27600-27607.
(20) Moggach, S. A.; Parsons, S.; Wood, P. A. High-pressure polymorphism in amino acids. *Crystallogr. Rev.* **2008**, *14*, 143-184.
(21) Dawson, A.; Allan, D. R.; Belmonte, S. A.; Clark, S. J.; David, W. I. F.; McGregor, P. A.; Parsons, S.; Pulham, C. R.; Sawyer, L. Effect of high pressure on the crystal structures of polymorphs of glycine. *Cryst. Growth Des.* **2005**, *5*, 1415-1427.
(22) Shinozaki, A.; Komatsu, K.; Kagi, H.; Fujimoto, C.; Machida, S.; Sano-Furukawa, A.; Hattori, T. Behavior of intermolecular interactions in α-glycine under high pressure. *J. Chem. Phys.* **2018**, *148,* 044507-1/8.
(23) Hinton, J. K.; Clarke, S. M.; Steele, B. A.; Kuo, I. F. W.; Greenberg, E.; Prakapenka, V. B.; Kunz, M.; Kroonblawd, M. P.; Stavrou, E. Effects of pressure on the structure and lattice dynamics of α-glycine: A combined experimental and theoretical study. *CrystEngComm* **2019**, *21*, 4457-4464.
(24) Moggach, S. A.; Marshall, W. G.; Rogers, D. M.; Parsons, S. How focussing on hydrogen bonding interactions in amino acids can miss the bigger picture: a high-pressure neutron powder

diffraction study of ε-glycine. *CrystEngComm* **2015**, *17*, 5315-5328.
(25) Bull, C. L.; Flowitt-Hill, G.; De Gironcoli, S.; Küçükbenli, E.; Parsons, S.; Pham, C. H.; Playford, H. Y.; Tucker, M. G. ζ -Glycine: Insight into the mechanism of a polymorphic phase transition. *IUCrJ* **2017**, *4*, 569-574.
(26) Moggach, S. A.; Allan, D. R.; Clark, S. J.; Gutmann, M. J.; Parsons, S.; Pulham, C. R.; Sawyer, L. High-pressure polymorphism in *L*-cysteine: The crystal structures of *L*-cysteine-III and *L*-cysteine-IV. *Acta Crystallogr. Sect. B Struct. Crystallogr. Cryst. Chem.* ***2006****, 62*, 296-309.
(27) Minkov, V. S.; Krylov, A. S.; Boldyreva, E. V.; Goryainov, S. V.; Bizyaev, S. N.; Vtyurin, A. N. Pressure-induced phase transitions in crystalline *L*- and *DL*-cysteine. *J. Phys. Chem. B* **2008**, *112*, 8851-8854.
(28) Minkov, V. S.; Goryainov, S. V.; Boldyreva, E. V.; Görbitz, C. H. Raman study of pressure-induced phase transitions in crystals of orthorhombic and monoclinic polymorphs of *L*-cysteine: Dynamics of the sidechain. *J. Raman Spectrosc.* **2010**, *41*, 1748-1758.
(29) Madden, J. J.; McGandy, E. L.; Seeman, N. C. The crystal structure of the orthorhombic form of *L*-(+)-histidine. *Acta Crystallogr. Sect. B Struct. Crystallogr. Cryst. Chem.* **1972**, *28*, 2377-2382.
(30) Madden, J. J.; McGandy, E. L.; Seeman, N, C.; Harding, M. M.; Hoy, A. The Crystal Structure of the Monoclinic Form of *L*-Histidine. *Acta Crystallogr. Sect. B Struct. Crystallogr. Cryst. Chem.* **1971**, *28*, 2382-2389.
(31) Averbuch-Pouchot, M. T. Crystal structure of *L*-histidine phospite and a structure reinvestigation of the monclinic form of *L*-histidine. *Zeitschrift für Krist. - Cryst. Mater.* **1993**, *207*, 111-120.
(32) Nowell, H.; Barnett, S. A.; Christensen, K. E.; Teat, S. J.; Allan, D. R. I19, the small-molecule single-crystal diffraction beamline at Diamond Light Source. *J. Synchrotron Radiat.* **2012**, *19*, 435-441.
(33) Merrill, L.; Bassett, W. A. Miniature diamond anvil pressure cell for single crystal x-ray diffraction studies. *Rev. SCI. Instrum.* **1974**, *45*, 290-294.
(34) Klotz, S.; Chervin, J.-C.; Munsch, P.; Le Marchand, G. J. Hydrostatic limits of 11 pressure transmitting media. *J. Phys. D Appl. Phys.* **2009**, *42*, 075413-1/7.
(35) Mao, H. K.; Bell, P. M.; Shaner, J. W.; Steinberg, D. J. Specific volume measurements of Cu, Mo, Pd, and Ag and calibration of the ruby R1 fluorescence pressure gauge from 0.06 to 1 Mbar. *J. Appl. Phys.* **1978**, *49*, 3276-3283.
(36) Oxford Diffraction / Agilent Technologies UK Ltd, Yarnton, E. CrysAlisPRO. Yarnton, Oxfordshire, UK. **2014**.
(37) Bruker AXS Inc., APEX3, Madison, Wisconsin, USA, **2017**.
(38) Winter, G. Xia2: An expert system for macromolecular crystallography data reduction. *J. Appl. Crystallogr.* **2010**, *43*, 186-190.
(39) Bruker AXS Inc., SADABS, Madison, Wisconsin, USA, **2001**.
(40) Sheldrick, G. M. SHELXT - Integrated space-group and crystal-structure determination. *Acta Crystallogr. Sect. A Found. Crystallogr.* **2015**, *71*, 3-8.
(41) Sheldrick, G. M. Crystal structure refinement with SHELXL. *Acta Crystallogr. Sect. C Struct. Chem.* **2015**, *71*, 3-8.
(42) Dolomanov, O. V.; Bourhis, L. J.; Gildea, R. J.; Howard, J. A. K.; Puschmann, H. OLEX2: A complete structure solution, refinement and analysis program. *J. Appl. Crystallogr.* **2009**, *42*, 339-341.
(43) McCandlish, L. E.; Stout, G. H.; Andrews, L. C. Statistics of derived intensities. *Acta Crystallogr. Sect. A* **1975**, *31*, 245-249.
(44) Lundgren, J. O.; Liminga, R. X-ray structure of ammonium perchlorate. I. X-ray data collection and estimation of variances of the intensities. *Acta Crystallogr. Sect. B Struct. Crystallogr. Cryst. Chem.* **1979**, *35*, 1023-1027.
(45) Clark, S. J.; Segall, M. D.; Pickard Ii, C. J.; Hasnip, P. J.; Probert, M. I. J.; Refson, K.; Payne, M. C. First principles methods using CASTEP. *Zeitschrift fur Krist. - Cryst. Mater.* **2005**, *220*, 567-570.

(46) Tkatchenko, A.; Scheffler, M. Accurate molecular van der Waals interactions from ground-state electron density and free-atom reference data. *Phys. Rev. Lett.* **2009**, *102*, 073005-1/4.
(47) Monkhorst, H. J.; Pack, J. D. Special points for Brillouin-zone integrations. *Phys. Rev. B* **1976**, *13*, 5188-5192.
(48) Pack, J. D.; Monkhorst, H. J. "special points for Brillouin-zone integrations"-a reply. *Phys. Rev. B* **1977**, *16*, 1748-1749.
(49) Gavezzotti, A. Calculation of lattice energies of organic crystals: The PIXEL integration method in comparison with more traditional methods. *Zeitschrift fur Krist.* **2005**, *220*, 499-510.
(50) Gavezzotti, A. *Molecular Aggregation;* Oxford University Press: Oxford, UK, **2007**.
(51) Gavezzotti, A. Efficient computer modeling of organic materials. The atom–atom, Coulomb–London–Pauli (AA-CLP) model for intermolecular electrostatic-polarization, dispersion and repulsion energies. *New J. Chem*. **2011**, *35*, 1360-1368.
(52) Reeves, M.; Parsons, S.; Wood, P. A. MR_PIXEL. *J. Appl. Cryst*. **2020**. Accepted for publication.
(53) Frisch M. J., Trucks G. W., Schlegel H. B., Scuseria G. E., Robb M. A., Cheeseman J. R., Scalmani G., Barone V., Mennucci B., Petersson G. A., Nakatsuji H., Caricato M., Li X., Hratchian H. P., Izmaylov A. F., Bloino J., Zheng G. Sonnenberg J. L., Hada M., Ehara M., Toyota K., Fukuda R., Hasegawa J.,Ishida M., Nakajiama T., Honda Y., Kitao O., Naki H., Vreven T., Montgomery J. J. A., Peralta J. E., Ogliaro F., Bearpark M., Heyd J. J., Brothers E., Kudin K. N., Staroverov V. N., Kobayashi R., Normand J., Raghavachari K., Rendell A., Burant J. C., Iyengar S. S., Tomasi J., Cossi M., Rega N., Millam J. M., Klene M., Knox J. E., Cross J. B., Bakken V., Adamo C., Jamarillo J., Gomperts R., Stratmann R. E., Yazyey O., Austin A. J., Cammi R., Pomelli C., Ochterski J. W., Martin R. L., Morokuma K., Zakrewski V. G., Voth G. A., Salvador P., Dannenberg J. J., Dapprich S., Daniels A. D., Farkas Ö., Foresmann J. B., Ortiz J. V., Cioslowski J., Fox D. J. *Gaussian 16 Rev. C.01.* Wallingford, USA, **2016**.
(54) Hohenstein, E. G.; Sherrill, C. D. Efficient evaluation of triple excitations in symmetry-adapted perturbation theory via second-order Møller-Plesset perturbation theory natural orbitals. *J. Chem. Phys.* **2010**, *133*, 104107-1/7.
(55) Parrish, R. M.; Burns, L. A.; Smith, D. G. A.; Simmonett, A. C.; DePrince, A. E.; Hohenstein, E. G.; Bozkaya, U.; Sokolov, A. Y.; Di Remigio, R.; Richard, R. M.; Gonthier, J. F.; James, A. M.; McAlexander, H. R.; Kumar, A.; Saitow, M.; Wang, X.; Pritchard, B. P.; Verma, P.; Schaefer, H. F.; Patkowski, K.; King, R. A.; Valeev, E. F.; Evangelista, F. A.; Turney, J. M.; Crawford, T. D.; Sherrill, C. D. Psi4 1.1: An Open-Source Electronic Structure Program Emphasizing Automation, Advanced Libraries, and Interoperability. *J. Chem. Theory Comput.* **2017**, *13*, 3185-3197.
(56) Alvarez, S. A. A cartography of the van der Waals territories. *Dalt. Trans.* **2013**, *42*, 8617-8636.
(57) Press, W. H.; Teukolsky, S. A.; Vetterling, W. T.; Flannery, B. P. *Numerical Recipes in Fortran 77, The Art of Scientific Computing;* Cambridge University Press: Cambridge, UK, **1993**.
(58) MacRae, C. F.; Sovago, I.; Cottrell, S. J.; Galek, P. T. A.; McCabe, P.; Pidcock, E.; Platings, M.; Shields, G. P.; Stevens, J. S.; Towler, M.; Wood, P. A. Mercury 4.0: From visualization to analysis, design and prediction. *J. Appl. Crystallogr.* **2020**, *53*, 226-235.
(59) Spek, A. L. Structure validation in chemical crystallography. *Acta Crystallogr. Sect. D Biol. Crystallogr.* **2009**, *65*, 148-155.
(60) Cliffe, M. J.; Goodwin, A. L. PASCal: A principal axis strain calculator for thermal expansion and compressibility determination. *J. Appl. Crystallogr.* **2012**, *45*, 1321-1329.
(61) Gonzalez-Platas, J.; Alvaro, M.; Nestola, F.; Angel, R. EosFit7-GUI : a new graphical user interface for equation of state calculations, analyses and teaching. *J. Appl. Crystallogr.* **2016**, *49*, 1377-1382
(62) Groom, C. R.; Bruno, I. J.; Lightfoot, M. P.; Ward, S. C. The Cambridge structural database. *Acta Crystallogr. Sect. B Struct. Sci. Cryst. Eng. Mater.* **2016**, *72*, 171-179.
(63) Kitamura, M.; Furukawa, H.; Asaeda, M. Solvent effect of ethanol on crystallization and growth process of *L*-histidine polymorphs. *J. Cryst. Growth.* **1994**, *141*, 193-199.
(64) Supriya, S.; Sivan, S.; Srinivasan, K. Nucleation control and separation of stable and metastable

polymorphs of *L*-histidine through novel swift cooling crystallization process. *Cryst. Res. Technol.* **2018**, *53*, 1700239-1/9.
(65) Wantha, L.; Punmalee, N.; Sawaddiphol, V.; Flood, A. E. Effect of ethanol on crystallization of the polymorphs of *L*-histidine. *J. Cryst. Growth.* **2018**, *490*, 65-70.
(66) Bernstein, J.; Davis, R. E.; Shimoni, L.; Chang, N. L. Patterns in hydrogen bonding: functionality and graph set analysis in crystals. *Angew. Chem. Int. ed. Engl.* **1995**, *34*, 1555-1573.
(67) Funnell, N. P.; Dawson, A.; Francis, D.; Lennie, A. R.; Marshall, Wi. G.; Moggach, S. A.; Warren, J. E.; Parsons, S. The effect of pressure on the crystal structure of *L*-alanine. *CrystEngComm* **2010**, *12*, 2573-2583.
(68) Giordano, N.; Beavers, C. M.; Kamenev, K. V; Marshall, W. G.; Moggach, S. A.; Patterson, S. D.; Teat, S. J.; Warren, J. E.; Wood, P. A.; Parsons, S. High-pressure polymorphism in *L*-threonine between ambient pressure and 22 GPa †. *CrystEngComm* **2019**, *21*, 4444-4456.
(69) Bull, C. L.; Funnell, N. P.; Flowitt-Hill, G.; Parsons, S. **2015**. Unpublished data.
(70) Konar, S.; Michalchuk, A. A. L.; Sen, N.; Bull, C. L.; Morrison, C. A.; Pulham, C. R. High-pressure ptudy of two polymorphs of 2,4,6-trinitrotoluene using neutron powder diffraction and density functional theory methods. *J. Phys. Chem. C* **2019**, *123*, 26095-26105.
(71) Bull, C. L.; Funnell, N. P.; Pulham, C. R.; Marshall, W. G.; Allan, D. R. A new high-pressure polymorph of phosphoric acid. *Acta Crystallogr. Sect. B Struct. Sci. Cryst. Eng. Mater.* **2017**, *73*, 1068-1074.
(72) Varga, T.; Wilkinson, A. P.; Jorgensen, J. D.; Short, S. Neutron powder diffraction study of the orthorhombic to monoclinictransition in $Sc_2W_3O_{12}$ on compression. *Solid State Sci.* **2006**, *8*, 289-295.
(73) Drozd, V.; Garimella, S.; Saxena, S.; Chen, J.; Palasyuk, T. High-pressure Raman and X-ray diffraction study of β-and γ-polymorphs of aluminum hydride. *J. Phys. Chem. C* **2012**, *116*, 3808-3816.
(74) Singh, P.; Harbola, M. K.; Johnson, D. D. Better band gaps for wide-gap semiconductors from a locally corrected exchange-correlation potential that nearly eliminates self-interaction errors. *J. Phys. Condens. Matter.* **2017**, *29*, 424001-1/6.
(75) Jacobs, M. H. G.; Oonk, H. A. J. The Gibbs energy formulation of the a, b, and c forms of Mg_2SiO_4 using Grover, Getting and Kennedy's empirical relation between volume and bulk modulus. *Phys Chem Miner.* **2001**, *28*, 572-585.
(76) Cairns, A. B.; Goodwin, A. L. Negative linear compressibility. *Phys. Chem. Chem. Phys.* **2015**, 17, 20449-20465.
(77) Speziale, S.; Duffy, T. S. Single-crystal elastic constants of fluorite (CaF_2) to 9.3 GPa. *Phys. Chem. Miner.* **2002**, *29*, 465-472.
(78) Gray, T.; Whitby, M; Mann, N. Bulk Modulus for all the elements in the Periodic Table. <https://periodictable.com/Properties/A/BulkModulus.html> (accessed October 9th, **2020**).

For Table of Contents Use Only

The Effect of High Pressure on the Crystal Structures of Polymorphs of *L*-Histidine

Giulia Novelli, Helen E. Maynard-Casely, Garry J. McIntyre, Mark R. Warren and Simon Parsons

1. EaStCHEM School of Chemistry and Centre for Science at Extreme Conditions, The University of Edinburgh, King's Buildings, West Mains Road, Edinburgh, Scotland, EH9 3FJ, UK.

2. Australian Nuclear Science and Technology Organisation, New Illawarra Road, Lucas Heights, NSW 2234, Australia.

3. Diamond Light Source, Harwell Campus, Oxfordshire, OX11 0DE, UK

The naturally occurring amino acid *L*-histidine exists as orthorhombic and monoclinic polymorphs. The hydrogen bonds in each are similar in terms of distance and energy, yet the response to pressure differs partly because of symmetry.